Department of Physics and Astronomy
Heidelberg University

Master's thesis in Physics

submitted by

Prachi Nagpal

born in Panipat, India

2023

Nonlinear pulse compression in a dispersion tunable multi-pass cell

This Master's thesis has been carried out by Prachi Nagpal at the

Max-Planck-Institut für Kernphysik

under the supervision of

apl. Prof. Dr. José R. Crespo López-Urrutia

Nichtlineare Pulskompression in einer durchstimmbaren Mehrpasszelle

Die spektrale Verbreiterung von sub-200 fs Nahinfrarot-Frequenzkammpulsen erfolgt durch die Selbstphasenmodulation (SPM) in einer Herriott-type Multipasszelle (MPC). Diese Geometrie beruht auf einer periodischen Fokussierung des Strahls durch gekrümmte Spiegel, um bei jedem Durchgang durch ein Kerr-Medium eine kleine nichtlineare Phase zu akkumulieren. Dem Mehrplattenansatz zur spektralen Verbreiterung mit Quarzglas folgt eine zeitliche Nachkompression auf sub-100 fs mit gechirpten Spiegeln. Darüber hinaus wird der Fall der Selbstkompression, bei der die anomale Dispersion eines KDP Kristalls genutzt wird, um den SPM-induzierten positiven Chirp zu kompensieren, numerisch simuliert. Die Zelle ist so konzipiert, dass auch während des Bulk-Plate-Betriebs die Dispersion mit Hilfe des Gasdrucks, eingestellt werden kann. Außerdem wird der externe Zugang zur Optik durch selbstgebaute Drehdurchführungen ermöglicht. Im Gesamtkontext unserer Experimente führen kürzere Pulse zum einen zu einer höheren Ausbeute an extrem ultravioletten Licht und zum anderen zu einer besseren zeitlichen Auflösung für Multiphotonen-Ionisationsstudien.

Nonlinear pulse compression in a dispersion tunable multi-pass cell

Spectral broadening of sub-200 fs near-infrared frequency comb pulses is carried out using the process of self-phase modulation (SPM) in a Herriott-type multi-pass cell. This geometry involves periodic focusing of the beam by curved mirrors to accumulate a small nonlinear phase at each pass through a Kerr medium. The multi-plate approach towards spectral broadening with fused silica crystals is followed by temporal post-compression to sub-100 fs using chirped mirrors. In addition, the case of self-compression is numerically simulated, where the anomalous dispersion of a KDP crystal is utilized to compensate for the SPM-induced positive chirp. The cell is distinctly designed to allow dispersion tunability using pressurized gases even during bulk-plate operation. Furthermore, external access to the optics is facilitated by home-built rotary feedthroughs. With an enhanced peak intensity, these shorter pulses promise a better yield of extreme ultraviolet light, which is generated using intra-cavity high-harmonic generation that will be employed for the spectroscopy of highly charged ions, and improved temporal resolution of multi-photon ionization studies.

Contents

List of Figures

1 Introduction

## 1.1 Precision spectroscopy of highly charged ions

Similar to a microscope exploring the quantum realm, laser spectroscopy strives for increasingly higher levels of resolving power. Each improvement in resolution provides a window into the intricate influences that fundamental interactions exert on the atomic wavefunction, unveiling subtle effects that shape our understanding of the quantum world.

Over the past few decades, significant technological advancements have propelled laser spectroscopy of neutral atoms and singly charged ions to remarkable levels of precision. State-of-the-art laboratories have achieved an unprecedented fractional uncertainty in frequency measurement, reaching the order of 10^{-18} [1]. Despite these remarkable achievements, further progress has been hindered by external disturbances arising from stray electric and magnetic fields, which are challenging to eliminate completely. To address this issue, one promising solution lies in the utilization of highly charged ions (HCIs). These ions exhibit a unique characteristic wherein the valence electrons are significantly more tightly bound to the nucleus compared to neutral or singly charged counterparts. Consequently, the electron cloud of HCIs displays reduced sensitivity to the aforementioned external perturbations. This enhanced stability opens up new avenues for advancing the precision of timekeeping [2].

Moreover, HCIs offer an additional advantage by presenting an increased sensitivity to phenomena that go beyond the predictions of the Standard Model in physics. These phenomena encompass the potential variations of fundamental constants and the opportunity to conduct tests of local Lorentz invariance, a fundamental principle of relativity. These ions are prevalent in astrophysical environments such as stellar coronae, accretion disks, and supernova remnants. They play a crucial role in various processes, including radiative emission and absorption, plasma heating and cooling, and energy transport. The spectroscopic analysis of HCIs observed in astronomical findings provides insights into the physical conditions and dynamics of these extreme environments [3, 4]. The interplay between precision measurements, technological advancements, and fundamental physics research in this field holds great potential for further scientific breakthroughs [2].

The increase in positive charge results in a significant increment of the energy gap between distinct principal quantum numbers (n). This leads to the displacement of electronic transitions into the X-ray and the extreme ultraviolet (XUV) spectrum. Additionally, the enhanced charge induces fine-structure transitions among electronic orbitals sharing the same n value, thereby impacting the electronic characteristics. These transitions are caused by electron spin flips induced by relativistic effects and typically arise in the optical or XUV ranges.

In laboratory settings, working with HCIs necessitates the availability of practical sources for these species. From a spectroscopic perspective, an ideal scenario would involve a line-shaped radiation source of HCIs. However, compromises become necessary when it comes to HCI sources due to the substantial energy concentration that occurs during HCI production in target ensembles. The resulting HCIs exhibit high kinetic energies and temperatures [5]. Achieving stationary conditions can be challenging due to the presence of steep density and temperature gradients, which lead to rapid target expansion. Additionally,
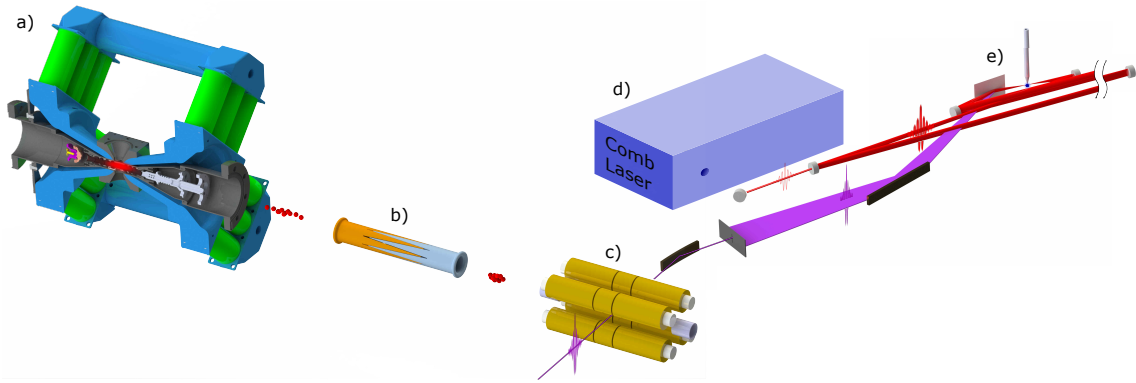
Figure 1.1: Schematic overview of the experimental setup for XUV spectroscopy of HCIs. a) The ions are produced in a miniature electron beam ion trap (EBIT). b) They are then bunched and decelerated using an electrodynamic pulsed drift tube [6] before they can be trapped in a c) linear Paul trap. d) The near-infrared (NIR) frequency comb pulses are amplified in e) a passive enhancement cavity, generating XUV pulses which are coupled out with a grating mirror and directed to the trap for direct frequency comb spectroscopy of HCIs. Figure from [7].

the differing mobilities of electrons and ions in plasma generate strong electromagnetic fields that evolve rapidly over time. Transient sources, such as those utilizing electrical discharges or laser-produced plasmas, are limited by these factors.

Fortunately, these challenges can be effectively overcome with the utilization of an electron beam ion trap (EBIT). As indicated by its name, it utilizes an intense beam of electrons. Within the trapping region (Figure 1.1 a.), the electron beam is compressed by a strong magnetic field, which counteracts the expansion caused by the repulsion between the electrons. This compression results in a highly dense beam that induces a negative space charge potential, and current densities reaching values of thousands of amperes per square centimeter. Under typical operational conditions, the potential difference between the central axis and the boundary of the electron beam ranges from tens to hundreds of volts [8]. In an EBIT, HCIs are typically produced through energetic collisions, with electron impact ionization being the most efficient mechanism [5]. The longitudinal confinement of the ions is provided by a set of drift tubes. Their charge state increases until the energy of the incoming electrons is no longer sufficient to reach the next charge state.

To attain remarkable performance in spectroscopy, several crucial requirements must be met:

1. Selection of an ion with a well-defined spectroscopy transition that is narrow and minimally affected by environmental perturbations.

2. Cooling techniques that effectively reduce the velocity-induced frequency shifts of the ions.

3. Reliable methods for preparing the atoms in a well-defined initial state.

4. Efficient techniques for detecting and measuring the states of the ions.

Interestingly, two different atomic species can share these requirements, so that one species need only have a good spectroscopy transition, and the other species can fulfill the other

three requirements. Such spectroscopy, called quantum logic spectroscopy, has been demonstrated with trapped atomic ions using quantum logic, a technique for precision atomic spectroscopy that removes the requirements of efficient cooling, state preparation, and state detection from the species upon which the spectroscopy is performed [9]. This approach makes it possible to read out the electronic state of an ion which does not possess a suitable transition for electron shelving, i.e. detection, on its own. Our experiment in the group led by J. R. Crespo López-Urrutia aims to utilize this approach for the XUV spectroscopy of HCIs. The schematic overview of the experiment is shown in Figure 1.1. The HCIs are produced in a compact EBIT, decelerated, and trapped in a cryogenic linear Paul trap together with laser-cooled beryllium ions for sympathetic cooling and state readout [10]. The fundamental frequency of a NIR frequency comb spectrum is passively amplified in a resonant cavity to generate the XUV light using high-harmonic generation (HHG) for direct frequency comb spectroscopy of HCIs.

Resonance frequencies in the XUV range are of great significance in various atomic and molecular systems in addition to ours. However, studying these systems has been challenging due to limitations in laser technology and the historical absence of long-term phase coherence in radiation sources in this frequency range. Recent advancements in XUV frequency comb technology have revolutionized spectroscopy by achieving remarkable resolution at the megahertz level [11–14].

1.2 Extreme ultraviolet frequency comb

A frequency comb is a phase-stabilized mode-locked laser. The optical pulses from mode-locked lasers, as demonstrated in Figure 1.2, result from the coherent addition of hundreds of thousands to millions of resonant longitudinal optical cavity modes. While the wide optical bandwidth of mode-locked optical spectra holds immediate appeal for spectroscopic applications, it also possesses unique properties that greatly benefit precision optical metrology. Firstly, all the optical modes within the spectrum are harmonically related, meaning they are perfectly equidistant in frequency. Secondly, these modes exhibit phase coherence with one another, sharing a common phase evolution. This yields notable outcomes: the electric field's evolution and the phase and frequency dynamics of every optical mode in the laser optical frequency comb (OFC) spectrum follow a deterministic pattern. Consequently, knowledge about the absolute frequency of one mode can be utilized to determine the absolute frequency of any other mode within the spectrum [15].
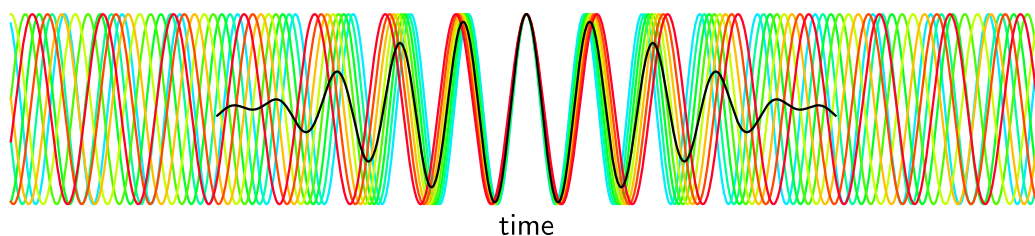
time

Figure 1.2: Depiction of mode-locking in the time domain. Longitudinal modes of the laser resonator with varying frequencies (depicted in different colors) with a fixed phase relationship interfere constructively. This gives rise to a short pulse (shown as a normalized pulse in black). Figure from [16].
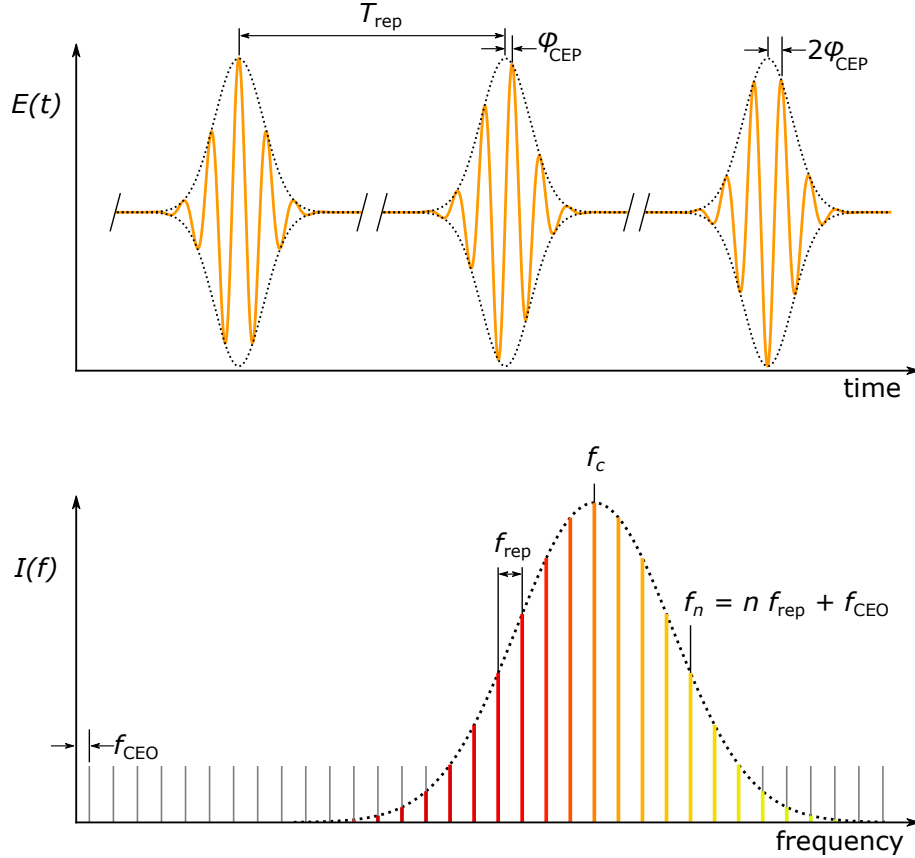
Figure 1.3: Time (top) and frequency (bottom) domain representation of an optical frequency comb. The interval between successive pulses, spaced at the repetition time $T_{\text{rep}} = 1/f_{\text{rep}}$, leads to a shift in the carrier phase under the envelope by an amount denoted as φ_{CEP}. The spectrum of the frequency comb showcases distinct and precise frequency peaks known as "comb teeth". The central point of the spectral envelope aligns with $f_{\text{c}} = \omega_c/2\pi$. Figure from [16].

We now delve into the relatively simple mathematics that characterizes the optical field output from a mode-locked laser. The optical field of the laser pulse train can be represented by a carrier frequency, $f_{\text{c}} = \omega_c/2\pi$, which is modulated by a periodic pulse envelope, $A(t)$. Typically, the time between optical pulses ranges between 1 and 10 ns. Due to the pulse periodicity, the optical field can also be described as a periodic Fourier series of optical modes, $f_N = \omega_N/2\pi$, with Fourier amplitude components A_N, and mode number N, such that

$$E(t) = A(t)e^{i\omega_c t} = \sum_{N=N_i}^{N_f} A_N e^{i\omega_N t}. \tag{1.1}$$

Since f_{c} is not necessarily an exact multiple of the mode spacing, f_{rep}, the individual Fourier frequencies are shifted from integer multiples of f_{rep} by a common offset, $f_{\text{CEO}} \leq f_{\text{rep}}$, such that

$$f_N = N \cdot f_{\text{rep}} + f_{\text{CEO}}. \tag{1.2}$$

Here, N is an integer mode number ranging from typically 100,000 to 1,000,000, which scales f_{rep} from the microwave domain to the optical domain. The deterministic behavior

of the OFC spectrum described above is most succinctly expressed by Equation 1.2.

It states that although an OFC consists of up to a million optical modes spanning hundreds of terahertz in the optical domain, only two degrees of freedom are required to define the frequency of each optical mode, f_N: first, the repetition rate, f_{rep}, and second, the laser offset frequency, f_{CEO}. This ability to fully define optical frequencies in terms of microwave frequencies was the original breakthrough of OFCs in precision optical metrology. To summarize, mode-locked lasers enable coherent division of optical frequencies to the microwave domain, and coherent multiplication of microwave frequencies to the optical domain [15].

The microwave mode that harmonically links the spectrum is the laser repetition rate, f_{rep}, which is the inverse of the pulse-to-pulse timing, T_{rep}. Pulses exit the laser cavity once per round trip, and the pulse repetition period, $T_{rep} = 2L/v_g$, where v_g is the pulse group velocity in the laser cavity, is defined and controlled by adjusting the laser cavity length, L. The harmonic and coherent connection between laser modes manifests as a common additive frequency offset, f_{CEO}. In the frequency domain, f_{CEO} shifts all the laser modes simultaneously. As f_{CEO} represents coherence, it is also related to changes in the optical carrier phase relative to the pulse envelope.

While it is not possible to directly count optical frequencies, optical frequency differences can be easily measured as long as they fall within the bandwidth limit of precision frequency counters (< 10 GHz). As a simple example, let's consider two optical carriers, f_1 and f_2, that are close in frequency. These carriers can be interfered to produce an optical carrier with amplitude modulation at the difference frequency, $\Delta f = f_1 - f_2$. When this signal is incident on a photodetector, the detector generates a voltage proportional to the amplitude modulation. In the literature, this signal is often referred to as a heterodyne optical beat frequency. The technique of measuring the difference frequency lies at the core of nearly all measurement methods involving optical OFCs, providing access to its characteristic frequencies, f_{CEO} and f_{rep}.

The direct conversion of optical frequencies to the microwave domain and vice versa marked a significant leap in precision metrology capabilities. In the first four years following their realization, a multitude of applications were swiftly demonstrated with OFCs. These included carrier-envelope phase control [17], the development of all-optical atomic clocks [18], absolute optical frequency measurements, and optical atomic frequency ratio measurements [19], among many others.

Shortly after the initial construction of frequency combs, the enhanced efficiency of nonlinear processes, facilitated by the high peak intensity of ultrashort pulses, was utilized to transfer the near-infrared (NIR) comb spectrum to various spectral regions. At first, the generation of XUV light using the principle of high-harmonic generation (HHG) was limited to low repetition rates and amplified ultrashort laser pulses, due to the requirement of very high intensities for this highly nonlinear process [20–22]. However, a significant breakthrough occurred in 2005 with the demonstration of the intra-cavity generation of high-order harmonics in a xenon gas target. This achievement was made possible by passively amplifying the NIR frequency comb pulses within femtosecond enhancement cavity (fsEC) [13, 23]. As a result, the fundamental comb spectrum was successfully extended to the XUV spectral region below 100 nm, filling the crucial gap and enabling a direct link between radio frequencies and XUV frequencies.
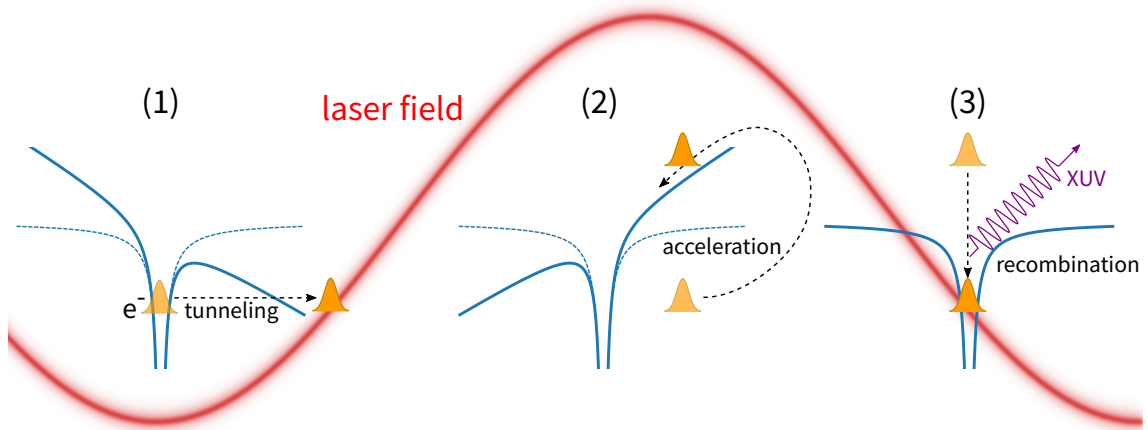
Figure 1.4: Schematic of the three-step model for HHG. 1) Ionization of an atom by a strong electromagnetic field, resulting in a free electron. 2) Subsequent acceleration of the free electron in the field, reversal of direction after half an optical period. 3) Return of the electron to the original ion, recombination under emission of a high energetic photon. Figure from [16].
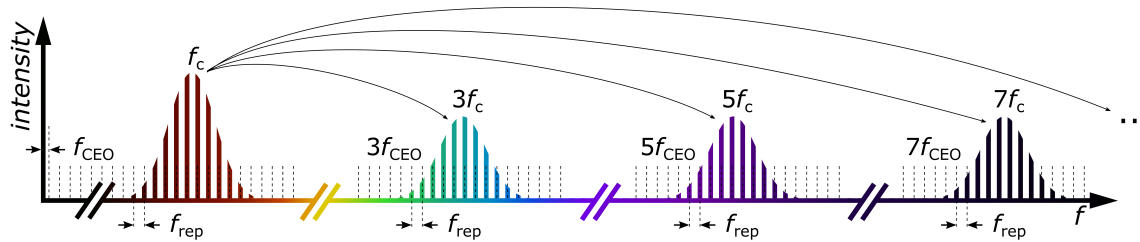
Figure 1.5: Transfer of the frequency comb spectrum from NIR to XUV by cavity-enhanced HHG. Comb copies centered at odd multiples of the central wavelength of the original comb are produced. Figure from [16].

In atomic or molecular gases, HHG can be semi-classically described as a three-step process (as depicted in Figure 1.4) [24, 25]: first, near the maxima of the driving field's amplitude, an electronic wavepacket is tunnel-ionized from the parent atom; in the second step, the electronic wavepacket is accelerated and, after reversal of the sign of the electric field, it is redirected to the parent ion; finally, upon re-collision, the electron's kinetic energy is emitted in the form of high-frequency radiation.

Traditionally, ultra-short laser pulses are generated using low repetition rate amplifier systems that operate in the kilohertz range. However, for precise direct frequency comb spectroscopy, the spacing between the comb lines should be wider than the width of the transition being studied. This requires a high repetition rate for the comb laser, which determines the frequency spacing. But generating high average power at multi-megahertz repetition rates, which is necessary to initiate highly nonlinear processes, remains a challenge. The development of stabilized laser systems capable of producing ultrashort pulses at such high average power levels is still underway. To overcome this technical hurdle, in our XUV frequency comb lab at the Max-Planck-Intitut für Kernphysik, passive amplification of a frequency comb in the NIR in a fsEC is employed to nonlinearly transfer the NIR spectrum to the XUV, as shown in Figure 1.5.

1.3 Motivation for pulse compression

The cavity-enhanced NIR frequency comb in our lab serves a dual purpose: generating high-harmonics for precision spectroscopy and studying nonlinear interactions between intense laser pulses and atoms [7, 16, 26]. By employing multiple photons, the comb's highly intense pulses enable the excitation and ionization of atoms. Multi-photon ionization (MPI) is a highly nonlinear process, that requires high laser intensities usually achieved through ultrashort pulses with kilohertz repetition rates [27, 28]. The ionization rate is proportional to I^n, where I is the laser intensity and n is the photon number. However, studying MPI at low intensities is challenging due to the drop in the count rate. To overcome this, our laser and fsEC operate at a 100 MHz repetition rate, allowing MPI studies at half the intensity compared to traditional systems but still achieving the same count rates. To visualize and measure the angle-resolved momentum distribution of charged particles, the velocity-map imaging (VMI) technique is used.

Both HHG and MPI are characterized by their highly nonlinear nature, making them extremely sensitive to even slight increases in laser intensity, and significantly increasing their yield. Hence, the spectral broadening of our almost-Fourier limited NIR pulses becomes imperative for temporal compression. In addition to being higher in intensity, a shorter pulse has a reduced number of electric field cycles. This enhances the efficiency of HHG as fewer cycles minimize plasma formation due to target gas ionization before the pulse reaches its intensity peak [29].

The use of shorter pulses also facilitates the attainment of higher photon energies and enables the study of MPI in atoms with larger ionization potentials. Time-resolved experiments can also be studied with enhanced resolution. Moreover, shorter pulses exhibit broader spectra, offering extended spectral coverage that is beneficial for various spectroscopic applications. This approach allows for the utilization of more frequency comb lines hence enabling access to a wider range of HCI transitions. But, direct few-cycle pulse generation from any power-scalable laser architecture is not in sight yet, and hence external pulse compression has been essential to reach the ultrashort pulse regime.

However, reducing the pulse duration requires spectral broadening, as the Fourier transform imposes a lower limit on pulse duration for a given spectral width. To address this, a dispersion tunable multi-pass cell (MPC) has been designed, which utilizes pressure-tunable dispersion compensation to nonlinearly broaden the laser spectrum [16, 30]. By effectively broadening the laser spectrum and temporally compressing the pulses, the MPC technology offers a pathway toward reaching even higher intensities and also enhancing the scope of various scientific investigations in our lab.

This thesis documents the experimental measurements of spectral broadening and pulse compression using the MPC. In the next chapter, the basic theory of the nonlinear process responsible for spectral broadening and pulse compression is discussed. In addition, numerical simulations of how the pulses propagate in a nonlinear medium are described with their results. Chapter 3 provides more details about the distinct design and features of the MPC. Lastly, Chapter 4 delves into the achieved results, ongoing improvements, and the future perspective.

2 Fundamentals of nonlinear optics

Nonlinear science is intriguing and widespread. While linear science often has established techniques to solve specific problems, nonlinearity can produce emergent phenomena where the whole is greater than the sum of its parts, making standard techniques rarely applicable. Even within a non-stochastic framework, the field can be unpredictable and welcome the emergence of qualitatively new phenomena, leading to exceptional outcomes for basic and applied sciences.

Nonlinear optics is a distinctive and diverse subset of nonlinear science. Although nonlinear effects in optics have been known for a long time, modern nonlinear optics was born with the invention of the optical maser, now known as the laser. Second-harmonic generation was demonstrated in 1961 by Franken and colleagues by tightly focusing a pulsed ruby laser into crystalline quartz [31]. After that, many nonlinear effects in light-matter interaction were experimentally demonstrated. They often quickly found their way into market applications in several different fields, ranging from telecommunications [32] to imaging for healthcare [33].

This is still an exciting research field with important and sometimes surprising outcomes for optical communications and optical sensing with new fascinating phenomena like rogue waves [34]. Nonlinear optics has also deeply dived into nanotechnologies and nanophotonics in the last 20 years, in line with what Richard Feynman said at the annual American Physical Society meeting in 1959, that there is still plenty of room at the bottom.

This chapter delves into the theory of self-phase modulation (SPM), explaining its role in the spectral broadening of ultrashort pulses. It also explores how dispersion affects these pulses. Simulation methods for pulse propagation in the MPC are introduced, followed by a presentation of their results.

2.1 Optical susceptibility

Nonlinear optics explains the nonlinear response of properties such as frequency, polarization, phase, or path of incident light. These nonlinear interactions give rise to a host of optical phenomena. Its origin is the nonlinear response of the material to external electric fields. The material response is manifest in the susceptibility. In general, the susceptibility is a tensor and the vector component of the fields must be taken into account, but here it is considered a scalar for simplicity. The linear susceptibility is related to the refractive index through

$$\chi_1 = n_0{}^2 - 1. \tag{2.1}$$

When intense light enters a transparent material, its susceptibility can become nonlinear. It is usually sufficient to consider this heuristically as a Taylor expansion in the electric field E

$$\chi(E) = \chi_1 + \chi_2 E + \chi_3 E^2 + \chi_4 E^3 + \dots. \tag{2.2}$$

All higher orders beyond χ_1 represent the nonlinear response of a material in the presence of intense light. The higher-order terms fall off in magnitude very rapidly unless the light

intensity is very high. The effect of the susceptibility on the light traveling through the medium is showcased in the polarization density P, where

$$P = \epsilon_0(\chi_1 E + \chi_2 E^2 + \chi_3 E^3 + ...). \tag{2.3}$$

The first-order term leads to a linear refractive index, as written in Equation 2.1. The second-order term is responsible for second-harmonic generation. For crystals with a center of symmetry and also for optically isotropic glasses, there is an absence of a second-order susceptibility. Hence, the lowest-order nonlinearity is caused by the third-order susceptibility. Assuming that the electric field is linearly polarized in one direction, the nonlinear polarization can be expanded as

$$P_3 = \frac{1}{8}\epsilon_0\chi_3\left(Ee^{i\omega t} + E^*e^{-i\omega t}\right)^3 \tag{2.4a}$$

$$= \frac{1}{8}\epsilon_0\chi_3\left(E^3 e^{i3\omega t} + E^{*3}e^{-i3\omega t} + 3E^2 E^* e^{i\omega t} + 3EE^{*2}e^{-i\omega t}\right) \tag{2.4b}$$

$$= \frac{1}{8}\epsilon_0\chi_3\left(\left(E^3 e^{i3\omega t} + c.c.\right) + 3|E|^2\left(Ee^{i\omega t} + c.c.\right)\right) \tag{2.4c}$$

where ϵ_0 is the vacuum permittivity. In the nonlinear response, there is an oscillation at thrice the fundamental frequency 3ω, and also at the fundamental frequency ω with the coefficient χ_3. Third-harmonic generation requires phase matching and we assume that this is not fulfilled. Hence we can neglect the first term in Equation 2.4c. Combining with the linear response, the total induced polarization is then

$$P = \epsilon_0\chi_1 E + \epsilon_0\chi_3 E^3 = \epsilon_0\left(\chi_1 + \frac{3}{4}\chi_3|E|^2\right)E. \tag{2.5}$$

χ_3 is typically fifteen orders smaller than χ_1. But at very high intensities, the product $\chi_3|E|^2$ can contribute to the polarization.

2.1.1 Nonlinear refractive index

The modified refractive index n, considering the contribution from χ_3 can be written as

$$n = \sqrt{1 + \chi_1 + \frac{3}{4}\chi_3|E|^2} \tag{2.6a}$$

$$= n_0\left(1 + \frac{3}{4n_0^2}\chi_3|E|^2\right)^{\frac{1}{2}} \tag{2.6b}$$

$$= n_0 + \frac{3}{8n_0}\chi_3|E|^2 \tag{2.6c}$$

$$= n_0 + \frac{3}{4\epsilon_0 cn_0^2}\chi_3 I \tag{2.6d}$$

$$= n_0 + n_2 I. \tag{2.6e}$$

where n_0 is the linear refractive index defined in Equation 2.1. Assuming $|E|^2$ is small, Taylor expansion of Equation 2.6c gives Equation 2.6d. The nonlinear component of the

refractive index is called n_2,

$$n_2 = \frac{3}{4\epsilon_0 c n_0^2} \chi_3, \tag{2.7}$$

while the related susceptibility is χ_3. Thus, the third-order susceptibility causes both third-harmonic generation and an intensity-dependent change in the refractive index $n(I)$. It does not require a material without a center of inversion symmetry; all materials have χ_3 terms.

Several processes of practical importance occur as a result of the intensity-dependent refractive index. One of them is self-focusing. Self-focusing of light is the process in which an intense beam of light modifies the optical properties of a material medium so that the beam is caused to focus within the material [35]. This circumstance is shown schematically in Figure 2.1 a). Here we have assumed that n_2 is positive. As a result, the laser beam induces a refractive index variation within the material with a larger refractive index at the center of the beam than at its periphery. If the incident laser light is a Gaussian beam,
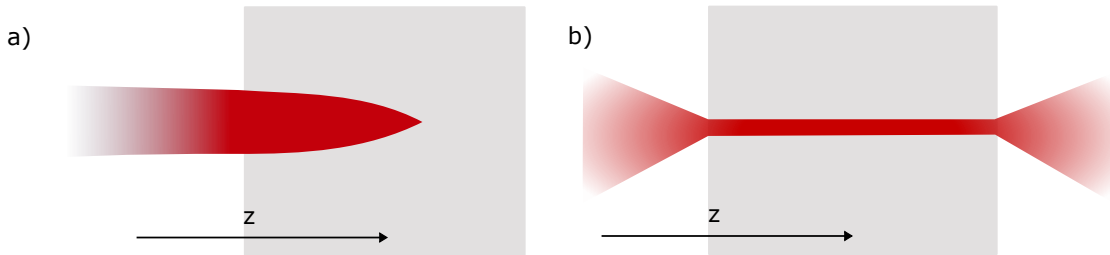
Figure 2.1: a) Self-focusing and b) Self-trapping of a laser beam that is propagating through a nonlinear medium (shaded rectangle) in the z-direction.

the nonlinear medium will induce a lateral spatially varying refractive index that will cause the beam to change its phase front. An intense light beam will tend to "self-focus" as it travels through the medium [35]. The nonlinear medium acts like a graded index lens. An exact treatment of short pulse self-focusing is complex as it involves the inclusion of many different nonlinear effects combined with propagation effects. The lateral change in beam shape due to the nonlinear refractive index motivated a new technique called the z-scan that can measure both the magnitude and sign of the nonlinear refractive index (as well as the nonlinear absorption) [36].

In the z-scan measurement technique, a sample of the nonlinear material is moved through the focus of a laser beam, and an aperture is placed before the detector at some point in the expanding beam. The amount of light getting through this aperture is measured as a function of the sample position. If the nonlinearity is positive, the beam tends to self-focus, reducing the beam divergence and increasing the amount of light transmitted through the aperture. If the nonlinearity is negative, the amount of light will decrease. From the measured dependence of the detector signal on the sample position, it is possible to calculate the magnitude of the nonlinear index.

In a broader sense, self-action effects are referred to as the phenomena in which a beam of light alters its own propagation by utilizing the nonlinear response of a material medium. Another example of a self-action effect is the self-trapping of light, depicted in Figure 2.1

b). This process involves the constant diameter propagation of a light beam, resulting from a delicate balance between self-focusing and diffraction effects. Upon analysis, it is revealed that self-trapping can only take place when the power carried by the beam precisely matches the critical power for self-trapping, where λ_0 represents the vacuum wavelength of the laser radiation. Therefore, it can be deduced from this line of reasoning that self-focusing can only occur if the beam power P exceeds P_{cr} [37].

$$P_{cr} = \frac{\pi(0.61)^2\lambda_0^2}{8n_0n_2}.$$ (2.8)

$P_{cr,FS} \approx 5\,\text{MW}$ for fused silica (FS) at 1039 nm. Examples of materials with higher nonlinearities are yttrium aluminium garnet (YAG) with $P_{cr,YAG} \approx 1.5\,\text{MW}$ and potassium dihydrogen phosphate (KDP) with $P_{cr,KDP} \approx 1.8\,\text{MW}$ [38].

Another self-action effect is the laser beam breakup. This phenomenon occurs when the beam power P is significantly greater than the critical power, disintegrating the beam into multiple components, each carrying approximately the power P_{cr}. This process is caused by the development of imperfections in the laser wavefront, which are amplified through the forward four-wave mixing process.

2.1.2 Transient nonlinear optics: self-phase modulation

Some phenomena occur only in the transient regime. These have become particularly important because ultra-short laser pulses (as short as femtoseconds) can provide changes in optical fields faster than any characteristic times in the system.

SPM is an important transient phenomenon. It relies on the fact that a pulse traveling through a nonlinear medium sees a time-dependent refractive index because the intensity changes over the time of the pulse. And a time-dependent refractive index introduces a time-variable phase shift that broadens the frequency spectrum of the pulse [39].

Let us consider the propagation of the optical pulse in accordance with the slowly varying envelope approximation in which the assumption is that the complex field amplitude $E_0(r,t)$ only varies slowly with r and t. This is valid when the spectral bandwidth is a small fraction of the carrier frequency. The field can then be written as a product of a fast oscillating part and a slowly varying envelope,

$$E(z,t) = A(z,t)e^{i(k_0z-\omega_0t)} + \text{cc}.$$ (2.9)

Here, $A(z,t)$ represents the envelope, and the oscillating part is described by the exponential term. If the pulse is traveling in a medium, the optical Kerr effect produces a refractive index change with intensity. As the pulse propagates, the intensity at any point in the medium first rises and then falls as the pulse goes past. Consequently, a time-varying refractive index is generated. This variation in refractive index produces a shift in the instantaneous phase of the pulse

$$\phi(t) = \omega_0t - \frac{2\pi}{\lambda_0}(n_0 + n_2I(t))z.$$ (2.10)

Because the output pulse has an additional phase modulation, its spectrum must have broadened. The phase shift leads to a change in the pulse's frequency spectrum. The

resulting instantaneous frequency is

$$\omega(t) = \frac{d\phi(t)}{dt} = \omega_0 - \frac{2\pi}{\lambda_0}(n_2 \frac{dI}{dt})z. \tag{2.11}$$
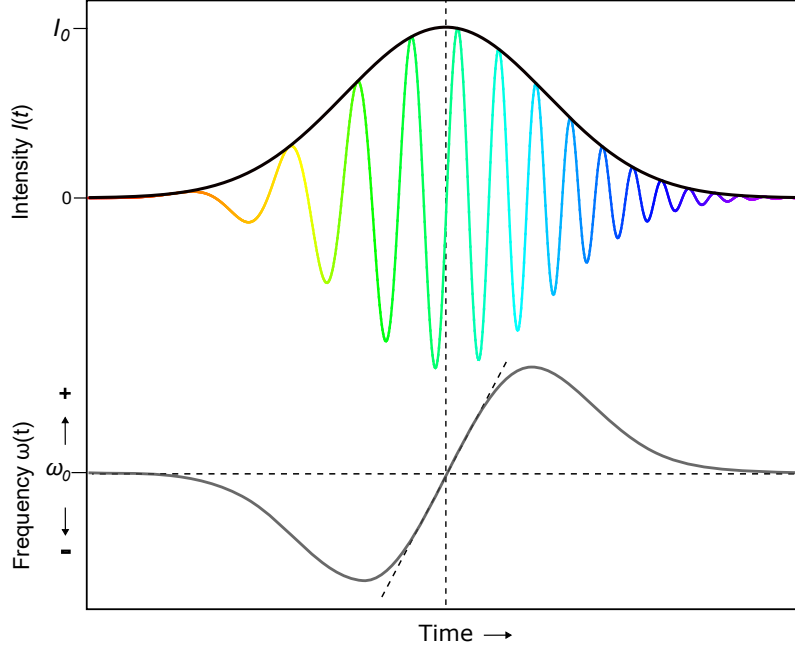
Figure 2.2: A pulse (Gaussian envelope marked by the black curve on top) propagating through a nonlinear medium undergoes a self-frequency shift (bottom grey curve) due to SPM. The front of the pulse is shifted to lower frequencies, and the back to higher frequencies, as shown by the rainbow colors. In the center of the pulse, the frequency shift is approximately linear.

Since the pulse under consideration is responsible for the time dependence of the phase response, this process is called SPM. Pure SPM broadens the frequency spectrum of the pulse, introducing a pure phase shift; it does not change the envelope of the pulse in the time domain.

Plotting $\omega(t)$ shows the frequency shift of each part of the pulse (Figure 2.2). The leading edge shifts to lower frequencies ("redder" wavelengths), the trailing edge to higher frequencies ("bluer"), and the very peak of the pulse is not shifted. For the center portion of the pulse (between $t = \pm\tau/2$, where τ is half the pulse duration), there is an approximately linear frequency shift (chirp) given by

$$\omega(t) = \omega_0 + \alpha t, \tag{2.12}$$

where α is

$$\alpha = \frac{d\omega}{dt}\bigg|_0 = \frac{4\pi z n_2 I_p}{\lambda_0 \tau^2}, \tag{2.13}$$

and I_p is the peak intensity of the Gaussian pulse.

Using femtosecond lasers in specially designed fibers, SPM can be so large as to produce a white-light continuum which has proven to be very useful for spectroscopy [40]. But all the frequencies travel at different speeds in the medium. In the context of pulse compression,

dispersion plays a crucial role in shaping the temporal profile of ultrashort laser pulses. Effective dispersion control mechanisms are essential for achieving high-quality compression and preserving pulse characteristics.

2.2 Dispersion in wave propagation

Dispersion is a fundamental property of optical systems that describes the wavelength dependence of the refractive index. In a short pulse, a broad range of frequencies or wavelengths are present, each with a different phase velocity in a given medium. As a result of dispersion, the individual spectral components of the pulse experience different delays, leading to temporal spreading and distortion of the pulse shape. In regions of normal dispersion, the "redder" portions of the pulse have a higher velocity than the "bluer" portions, and thus the front of the pulse moves faster than its back. In regions of anomalous dispersion, the opposite is true.

Different spectral components in the pulse propagate as per the relation

$$\tilde{A}(z, \omega) = \tilde{A}(0, \omega) \exp^{-i\beta z}, \tag{2.14}$$

where $\tilde{A}$ is the amplitude of the frequency component that accumulates a phase β as it propagates along the z direction. Phase accumulated by different frequency components is different and we can evaluate that as

$$\beta = \frac{\omega}{c} n(\omega). \tag{2.15}$$

Even though such phase changes do not affect the pulse spectrum, they can modify the pulse shape. Since β is a function of ω, the pulse experiences temporal broadening. Assuming that the pulse is such that $\Delta\omega < \omega_0$ (where $\Delta\omega = \omega - \omega_0$), a Taylor expansion can be done for $\beta(\omega)$ about ω_0,

$$\beta(\omega) = n(\omega)\frac{\omega}{c} \approx \beta_0 + \frac{d\beta}{d\omega}\bigg|_{\omega=\omega_0}(\omega-\omega_0) + \frac{1}{2}\frac{d^2\beta}{d\omega^2}\bigg|_{\omega=\omega_0}(\omega-\omega_0)^2 + \frac{1}{6}\frac{d^3\beta}{d\omega^3}\bigg|_{\omega=\omega_0}(\omega-\omega_0)^3 + ..., \tag{2.16}$$

where $\beta_1 = d\beta/d\omega|_{\omega=\omega_0}$ is defined as the group velocity, $\beta_2 = d^2\beta/d\omega^2|_{\omega=\omega_0}$ is defined as the group velocity dispersion (GVD), and $\beta_3 = d^3\beta/d\omega^3|_{\omega=\omega_0}$ is the third-order dispersion (TOD) parameter. The pulse can maintain its width only if all spectral components arrive together. Any time delay in the arrival of different spectral components leads to pulse broadening. As our goal is to compress pulses temporally, positive dispersion is undesired. Hence, to compensate for dispersion, a compressor is required. The chirp imposed by GVD is linear for Gaussian pulses and its spectral phase varies quadratically with frequency. A compressor is then simply an element with adjustable GVD, for example, a prism or grating sequence, provided higher-order dispersion can be neglected. However, even though second-order dispersion dominates, higher-order dispersion terms are unavoidable in all linear elements. These terms become more important as broader pulse spectra have to be handled. With such short pulses (100 fs), TOD plays an important role in limiting the pulse width and may impose a nonlinear chirp on the pulse. It introduces additional temporal distortions in the wave packet beyond simple broadening or compression, leading to complex pulse-shaping effects.
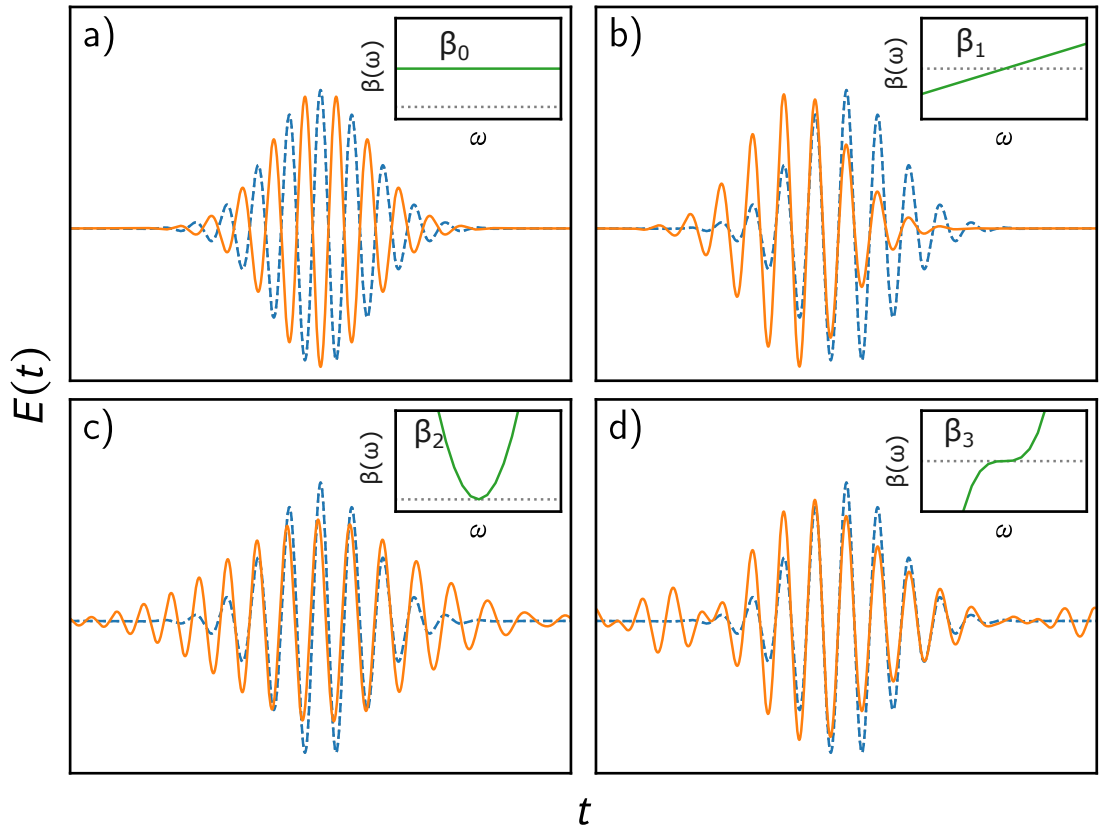
Figure 2.3: The blue dotted line shows a ten-cycle ultrashort laser pulse without dispersion. The spectral phase $\beta(\omega)$ modifies the electric field in the spectral domain resulting in a modified (temporal) electric field $E(t)$, drawn as a solid orange line. a)-d) show the effect of different orders of dispersion on the pulse. The corresponding spectral phase is plotted in the insets. Figure from [16].

The interplay of the GVD and SPM effects can lead to a qualitatively different behavior compared with that expected from GVD or SPM alone. If the pulse is intense enough, the positive chirp caused by SPM can be balanced by the negative chirp due to anomalous dispersion and reach an equilibrium state called an optical temporal soliton. In order to generate the shortest pulses, the pulse group delay after the phase modulator and the compressor must be nearly frequency independent.

For an initially unchirped Gaussian pulse, the dispersion-induced broadening broadens the pulse by the same amount in the normal- and anomalous-dispersion regimes. This behavior changes if the Gaussian pulse has an initial frequency chirp [41].

A practical limit for the achievable compression factor and pulse duration is given by the maximum power that can be propagated through the medium without causing damage. However, before this limit is reached, other nonlinear and linear effects have to be considered. These include TOD, Raman processes, the $|E|^4$ dependence of the refractive index, and the effect of a shock term in the wave equation.

Finally, with the knowledge of SPM and dispersion, we are equipped with the theory required to temporally compress short pulses. Experimentally, there are numerous ways

to do it. An intuitive way would be to implement spectral broadening in a bulk material. This exploits third-order nonlinearity in crystals of varying thicknesses depending on the required broadening ratios. But since high intensities are required to induce SPM, these high intensities also accompany self-focusing effects which limit the peak intensities that can be used depending on the damage threshold of the bulk medium. Another method is to use the nonlinearity of pressurized gases in a capillary [42] but it requires millijoule pulse energies and can only be used at relatively low repetition rates of the laser. A hollow core waveguide could be used [43], in which the small central core allows for very tight confinement of light. It has a diameter of just a few microns. So, by restricting light to propagate in a small volume, high intensities are achieved turning on the nonlinear optical effects. But there is a risk of destroying the fiber at the high average powers of the laser.

An ingenious method is propagation through a thin bulk plate multiple times [44]. This can be easily done in a Herriott-type configuration [45] which was first introduced in 1964. This is the general idea behind spectral broadening in an MPC. It is named so because the laser passes through the nonlinear medium multiple times. In this way, the nonlinearity is distributed over many passes and is thus spatially homogenized [46]. It is important to observe that effective spatio-temporal homogenization relies on selecting a sufficiently low value for the per-pass nonlinear phase. This is necessary to prevent substantial self-focusing and beam aberrations caused by the non-spherical shape of the Kerr-lens [44, 47].

In its simplest form, an MPC comprises a stable resonator with two mirrors and a mechanism for injecting and extracting light beams. By adjusting the MPC parameters correctly, the incident beam, when injected with the appropriate offset and tilt, undergoes multiple bounces within the cell before exiting [48]. These successive bounces of the beam, observed in a specific reference plane (such as one of the end mirrors), form an elliptical or circular spot pattern. With careful design considerations, the MPC can maintain the Gaussian beam's q parameter unchanged. This implies that diffractive beam spreading effects are precisely canceled out due to the periodic focusing occurring inside the cavity.

In pulse compression applications, the setups typically used for MPCs resemble the configuration shown in Figure 2.4. In q-preserving resonators, a telescope is employed to ensure that the laser beam is mode matched to their eigenmode, guaranteeing consistent beam properties per pass through the cell. This is discussed further below. Subsequently, the beam is directed off-axis to the MPC using a small scraper mirror [49]. Once the desired number of round trips has been achieved, the output beam, which has undergone spectral broadening, is extracted through the same scraper or hole in the mirror, or through an out-coupling mirror positioned on the opposite side of the cell [50]. The beam then requires collimation, and chirp removal is typically accomplished through a grating compressor or chirped mirror compressor. Alternatively, self-compression techniques that simultaneously compress the laser pulse within the spectral broadening stage can also be utilized [51].

2.3 Numerical modeling of nonlinear pulse propagation

Numerical simulations can be employed for fast scanning of the various interdependent parameters of the MPC. For that, the nonlinear effect of SPM that plays a significant role in pulse propagation must be included. Dispersion effects due to propagation in different media and reflection from the mirrors must also be added to the pulse. A simplified approach neglecting spatio-temporal couplings and self-focusing within the cell is followed [16, 30].

The calculation incorporates a Python open-source solver for the generalized nonlinear Schrödinger equation (GNLSE) [52], which is derived from code initially developed by J. M. Dudley and J. R. Taylor for studying supercontinuum generation in nonlinear optical fibers [53].

The nonlinear Schrödinger equation (NLSE) is a fundamental mathematical model that describes how the pulse amplitude envelope is shaped. It considers both the time and distance of propagation and incorporates important factors like second-order dispersion and SPM. The NLSE has been successfully employed in the modeling of picosecond pulse propagation in optical networks, particularly for low-energy pulses. However, when it comes to femtosecond high-energy pulses, the NLSE alone proves to be insufficient. To enhance the existing NLSE model, higher-order dispersion and expressions representing successive nonlinear processes, such as Raman scattering, have been included [52]. This improved model is known as the GNLSE. It takes the form

$$
\begin{aligned}
\frac{\partial A(z,T)}{\partial z} = &-\frac{\alpha}{2}A(z,T) - \sum_{k=2}^{\infty}\left(\frac{i^{k-1}}{k!}\beta_k\frac{\partial^k A(z,T)}{\partial T^k}\right) \\
&+ i\gamma\left(1 + \frac{i}{\omega_0}\frac{\partial}{\partial T}\right)A(z,T) + \int_{-\infty}^{\infty}R(T')\left|A(z,T-T')\right|^2 dT'.
\end{aligned}
\tag{2.17}
$$

It describes the evolution of the slowly varying time domain field amplitude $A(z,T)$ with a carrier wave oscillation frequency ω_0. In the above description, T corresponds to the local time of the pulse. Furthermore, spatio-temporal couplings are neglected, meaning that the spatial amplitude of the field is assumed to be separable from the temporal amplitude. α represents the attenuation constant, and β_k are the higher-order dispersion coefficients obtained by expanding the propagation constant $\beta(\omega)$ in a Taylor series around the center frequency ω_0. γ is the effective nonlinear coefficient that describes the influence of SPM on the pulse

$$
\gamma = \frac{n_2\omega_0}{c_0 A_{\text{eff}}},
\tag{2.18}
$$

where A_{eff} denotes the effective area of the intensity profile during the nonlinear interaction.

The temporal derivative $\partial/\partial t$ in the third term on the right-hand side of Equation 2.17 takes into consideration the higher-order nonlinear effects of self-steepening (the peak of the pulse travels at a speed different from that of the leading and trailing edge so that ultimately the pulse tries to form a shock at the trailing edge if n_2 is positive or on the leading edge if n_2 is negative). Finally, the first term in the second line of Equation 2.17 takes into account the nearly instantaneous electronic contribution of the Raman response, while the convolution integral describes the delayed Raman response and Raman gain of the material.

Equation 2.17 can be solved analytically only in particular cases, when either attenuation, dispersion, or nonlinearities are neglected. In general, a close-form solution does not exist and numerical simulations are commonly used to model the evolution of the optical signal. The split-step Fourier method is a numerical technique used to solve partial differential equations (PDEs), particularly those of the NLSE type. This method takes advantage of the fact that the Fourier transform can diagonalize linear operators, allowing to split the evolution equation into simpler components (linear and nonlinear) that can be solved

individually. By alternating between temporal and Fourier domains, the method efficiently simulates the evolution of the field. It can be described step-by-step as follows:

1. Discretization: The spatial domain is divided into a discrete grid with evenly spaced points. The field under consideration is represented by discrete values at these grid points.

2. Fourier Transform: The initial field is transformed from the temporal domain to the Fourier domain. This transformation provides its representation in terms of its spectral components.

3. Linear Evolution: The linear part of the PDEs, which usually involves derivatives and linear operators, is evolved in the Fourier domain. This is accomplished by multiplying the Fourier coefficients of the field by a corresponding phase factor, which incorporates the linear evolution of each spectral component.

4. Inverse Fourier Transform: The field is transformed back from the Fourier domain to the temporal domain.

5. Nonlinear Evolution: The nonlinear part of the PDEs, which typically involves products of the field, is evolved in the temporal domain.

6. Repeat: Steps 2-5 are repeated for each point in space. The iterative process allows for the accurate simulation of the field evolution over time.

By splitting the evolution equation into linear and nonlinear steps and utilizing the Fourier transform, the split-step Fourier method provides an efficient and accurate numerical solution to a wide range of nonlinear PDEs. It is particularly useful in simulating phenomena involving wave propagation, such as optical pulse propagation in fiber optics or soliton dynamics in nonlinear media. Hence we employ it in our case where a pulse propagates back and forth between two mirrors going through a nonlinear medium multiple times.

2.3.1 Simulation setup

In the MPC simulations, the pulse undergoes propagation within a geometry consisting of curved mirrors with a nonlinear material and gas between them. At each reflection on the mirrors and during propagation in the gas, dispersion effects are introduced. Nonlinear effects are specifically accounted for within the crystal. The length of the crystal is divided into smaller increments. Within each increment, the simulation sequentially incorporates nonlinear effects in the time domain and dispersion effects in the frequency domain. The Fourier transform is employed to establish the connection between the time and frequency domains as described before.

The propagation of femtosecond laser pulses in an optically transparent medium results in the alteration of its properties. We will examine the scenario where both linear and nonlinear effects are equally significant. Linear effects are associated with the wavelength-dependent refractive index, while nonlinear effects arise from the cubic nonlinearity of the medium. The linear effects can be described by the GVD parameter $\beta_2 = \left(d^2k_0/d\omega^2 \right)|_{\omega=\omega_0}$, whereas the nonlinear effects are quantified by the accumulated nonlinear phase or B-integral. The B-integral is a valuable measure used to quantify spectral broadening. In this context, loss- and dispersion-less propagation of a Gaussian beam within a symmetric
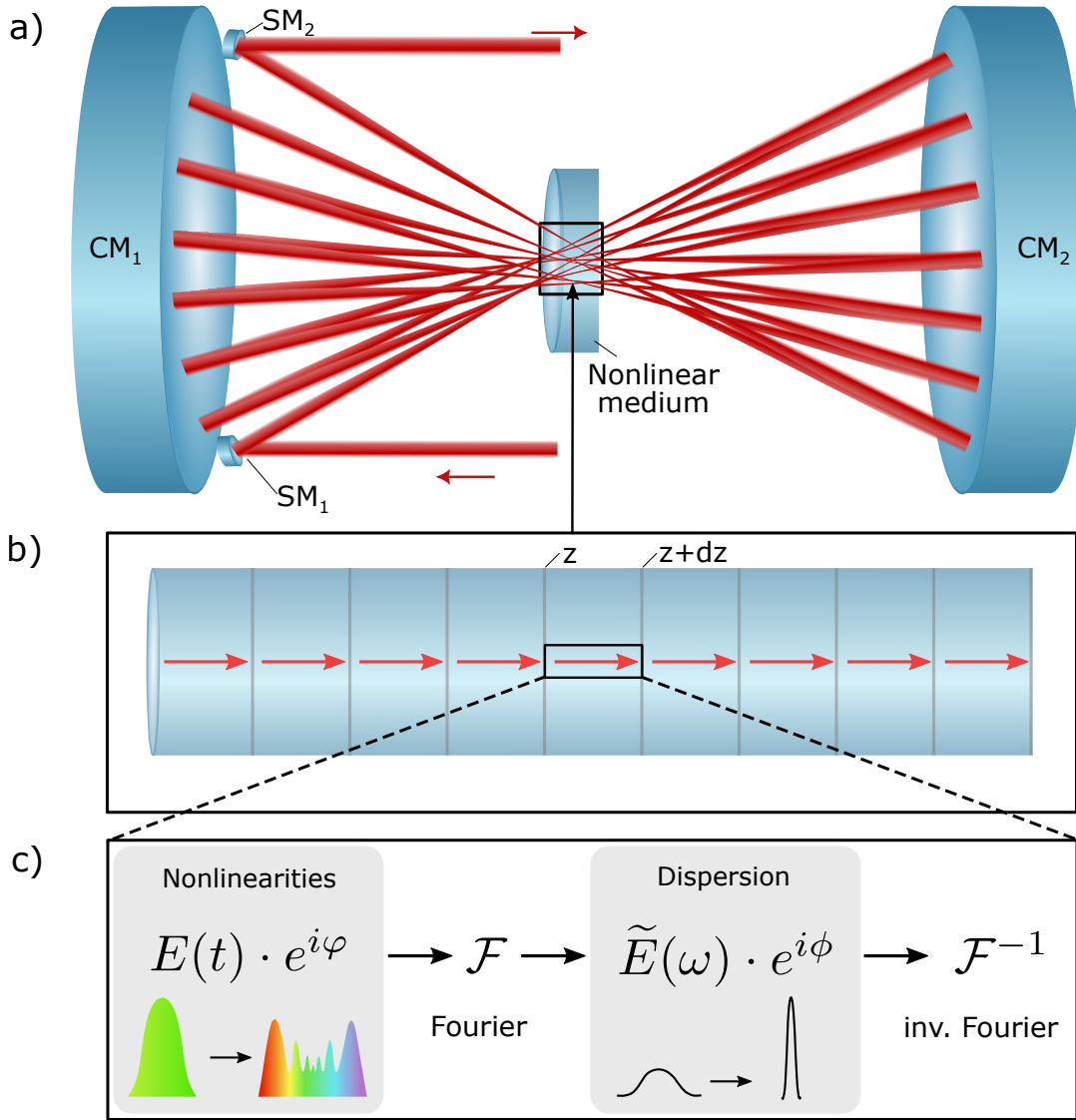
Figure 2.4: Schematic of the working principle of the split-step Fourier method employed to simulate spectral broadening in the MPC. a) A converging beam is coupled in the MPC using a scraper mirror (SM_1). The beam goes back and forth between the two curved mirrors (CM_1 and CM_2) in a Herriott geometry before it is finally coupled out with another scraper mirror (SM_2). b) The nonlinear medium (crystal in the center) is split into small steps of size dz. c) In each step, the nonlinearities are added in the time domain and dispersion in the frequency domain. Adapted from [16].

MPC, the single-pass integral [46] can be expressed as the accumulated on-axis nonlinear phase, denoted as B_{pass}

$$B_{\text{pass}} = 2\phi_{\text{max;pass}} = 4\pi \frac{n_2 P}{\lambda^2 z_R} \int_{d_k}^{d_k+l_k} (1 + z^2/z_R^2)^{-1} dz. \qquad (2.19)$$

Here, d_k represents the distance from the cell center to the Kerr medium, l_k denotes the length of the Kerr medium, and z_R represents the Rayleigh length.

We will consider two cases. The first case is when β_2 and n_2 have different signs. Such a situation occurs, for example, in a KDP (Potassium Dihydrogen Phosphate) crystal at room temperature ($\sim 300\,\text{K}$) if the wavelength of the ordinary wave $\lambda > 980\,\text{nm}$ [54]. The opposite signs of the parameters β_2 and n_2 allow the temporal self-compression. This regime involves simultaneous spectrum broadening and correction of the spectral phase of the pulse propagating in the nonlinear medium. The spectrum broadens due to SPM, while the phase correction occurs as a result of the anomalous dispersion of the linear part of the refractive index.

The second case is when β_2 and n_2 have the same sign. Such a situation occurs in the case of FS. For this case, the nonlinear material only broadens the spectrum, and temporal post-compression of pulses is required.

The crucial parameters for implementing temporal self-compression in an MPC include the beam shape, beam diameter, pulse energy, initial pulse duration, the maximum value of the B-integral, peak intensity, nonlinear length, number of passes through the medium, and desired level of temporal compression. In order to achieve temporal self-compression, it is necessary to optimize the peak intensity and length of the nonlinear medium, taking into account the specific value of the initial pulse duration. However, a significant limitation arises from the minimum possible diameter of the laser beam, as the length of the nonlinear crystal must be smaller than the length of disruptive self-focusing. The beam will collapse if this condition is not met, rendering further application impossible. The collapse length of a Gaussian beam with a radius w_0 (characterized by a transverse distribution $I \sim \exp-(r/R)^2$) can be obtained as an expression for the self-focusing length [37]

$$z_{\text{sf}} = w_0 \sqrt{\frac{n_0}{2n_2 I}} = \frac{2n_0 w_0^2}{\lambda} \frac{1}{\sqrt{P/P_{\text{cr}}}} \ (\text{for } P > P_{\text{cr}}). \qquad (2.20)$$

This value changes for small laser powers as the converging angle gets reduced by diffraction effects. In addition, with a reduction in duration after each pass and without significant energy loss, the length at which the laser beam collapses decreases.

2.3.2 Simulation results

In our simulations, we start with a Gaussian pulse of duration 185 fs with a pulse energy of 550 nJ. For the linear regime, a phase shift due to reflection at the mirrors, dispersion in the nonlinear medium, dispersion in air, vacuum, or over-pressure of any inert gas. Both gases and crystals can exhibit nonlinearities, which can be taken into account. For the first case of self-compression, we employ KDP which has anomalous dispersion at our wavelength of 1039 nm. For the chosen number of passes and beam waist at the center, as

is moderated by the experimental setup, one can simulate pulse compression for different thicknesses of KDP and pressures of gases.

Similarly for the second case with FS, the MPC simulation includes a post-compression setup with chirped mirrors. For a chosen amount of spectral broadening, one can simulate the number of reflections required on a set of chirped mirrors for desired temporal compression.

In the following pages, the simulation results are depicted. Each figure contains four subplots, the top two show the evolution of the pulses with an increasing number of passes through the nonlinear medium in the time and the spectral domain. The bottom two represent the peak power and the power spectral density of the input and output pulses. The comparative analysis between these parameters is done here to get an understanding of how a small change in these parameters greatly affects the outcome.
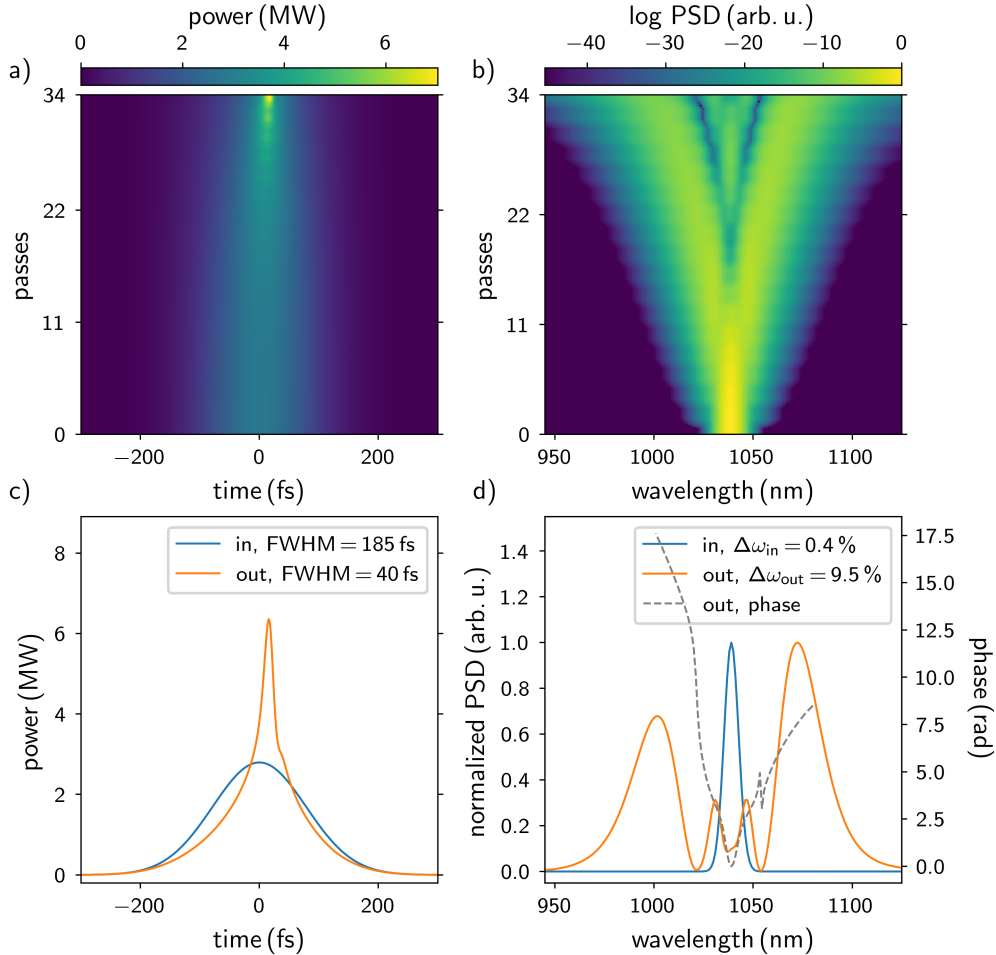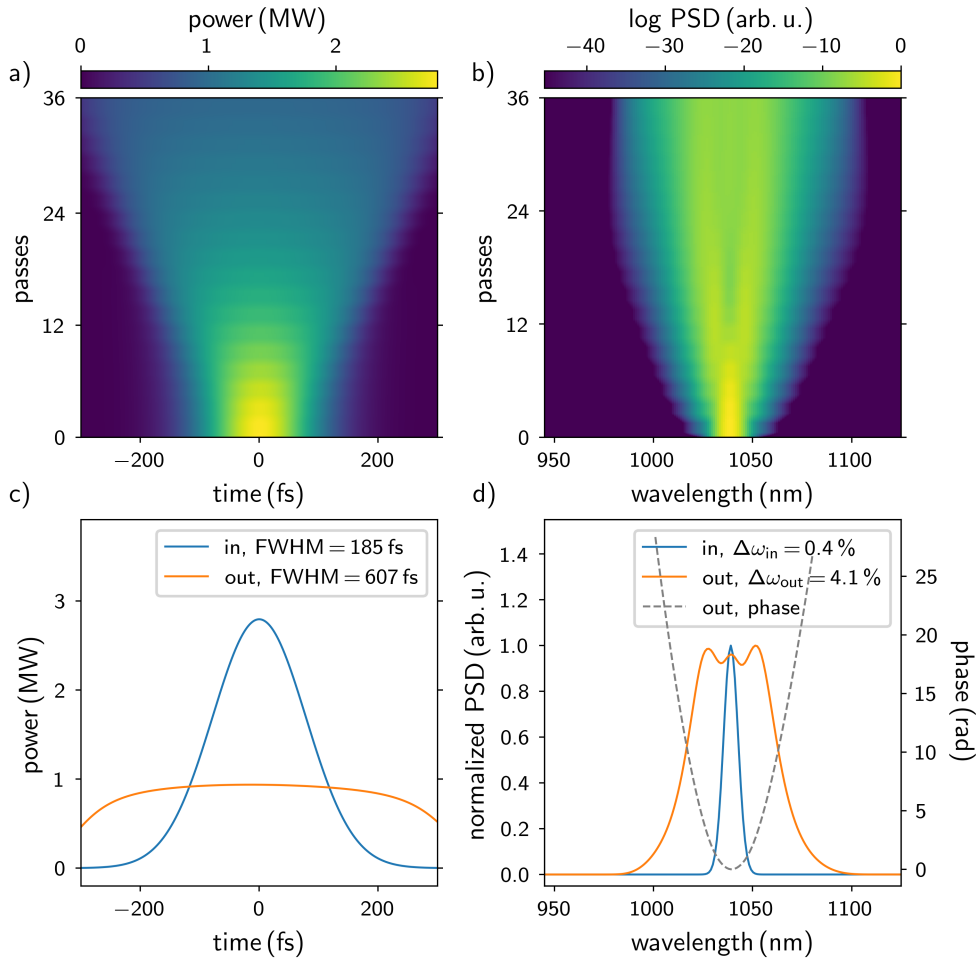

Figure 2.5: Simulation of propagation dynamics of pulses propagating through 5 mm thick KDP. The evolution of the pulse in the temporal and spectral domains is shown in a) and b), respectively. c) The out-coupled pulses are 40 fs short. d) After 34 passes, the pulses spectrally broaden by a factor of 27.

Simulation results with 5 mm KDP for 34 passes through the crystal at atmospheric pressure result in a spectral broadening by a factor of 27 and a temporal compression to 40 fs, as shown in Figure 2.5. Upon choosing a larger thickness of KDP or a narrower beam waist, fewer passes are required to get desired compression ratios. The critical power for self-focusing (Equation 2.8) must be taken care of in this case.

For FS as the nonlinear medium and normal mirrors as MPC mirrors, the cell does not compensate the chirp buildup. With each pass, the chirp gets enhanced. This results in spectral broadening without temporal compression.

It can be seen in Figure 2.6 where 15 mm of FS is used. With a beam waist of 90 μm at the crystal position, 36 passes are required to spectrally broaden by a factor of ~ 12 in the presence of ambient air.

Figure 2.6: Simulation results with 15 mm of FS. The evolution of the pulse in the temporal and spectral domains is shown in a) and b), respectively. c) The pulses are temporally broadened in this case and post-compression is required. d) Pulses are spectrally broadened by a factor of ~ 12.
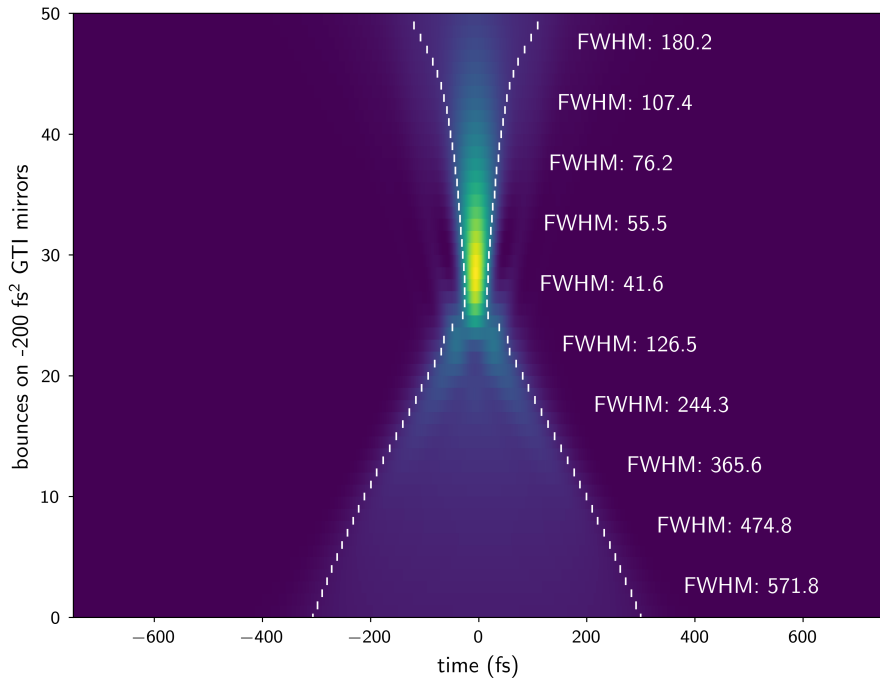
Figure 2.7: Simulation results of temporal compression using a chirped mirror post-compressor. The spectrally broadened pulses from Figure 2.6 are temporally compressed by Gires-Tournois-Interferometer (GTI) mirrors, each with a group delay dispersion (GDD) of $-200\,\text{fs}^2$. 27 bounces are required to compress the pulses to $\sim 41\,\text{fs}$. The GDD of the MPC mirrors, the outcoupling window, and the collimating lenses are ignored.

But a post-compression system can be simulated with chirped mirrors of GDD of each $-200\,\text{fs}^2$ as can be seen in Figure 2.7. After 27 bounces on the chirped mirrors, the pulses can be temporally compressed to 41.6 fs. It is quite evident that after a few passes, spectral broadening saturates. That is because peak intensities are not maintained due to the increasing temporal width of the pulses. Hence, in such a cell, it would be best to have as few passes as possible and avoid excessive dispersion due to propagation.

It is important to take into consideration the geometry of the cell as it puts constraints on the values of the simulation parameters. This is explained in detail in the next chapter.

3 Dispersion tunable multi-pass cell

3.1 Laser setup

The laser system is built around the Menlo Systems FC1000-250, a commercially available frequency comb that generates pulses with a duration of 24 ps centered at 1039 nm. The spectral bandwidth at the full width half maxima (FWHM) is 14 nm, and the repetition rate is 100 MHz. The oscillator comprises a Yb-doped fiber, with a short section of free space for offset and repetition rate adjustments. The repetition rate can be modified by up to 1%. To ensure repetition rate stability, the system is synchronized with a local 10 MHz resonator, which, in turn, receives atomic clock data via GPS. Consequently, the repetition rate can be locked to within a fractional uncertainty of 10^{-12} within a one-second interval.
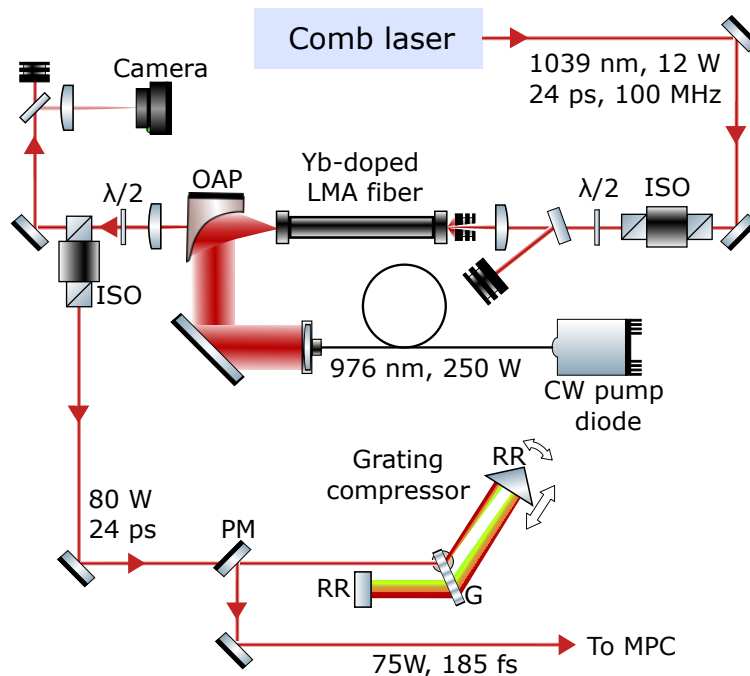
Figure 3.1: Schematic overview of the home-built amplifier and grating compressor setup. Stretched pulses from the commercial comb laser are amplified in a Yb-doped rod-type fiber amplifier. The picking mirror (PM) with a vertical offset reflects the compressed beam from the grating compressor towards the MPC for spectral broadening and post-compression. OAP: off-axis parabolic mirror, ISO: optical isolator, RR: Retroreflector. Adapted from [16].

The pulses are subsequently amplified using a home-built setup [7, 16], as shown in Figure 3.1, based on chirped pulse amplification [55]. In chirped pulse amplification, pulses are temporally stretched by dispersion prior to amplification. After amplification, temporal re-compression yields pulses with high peak power after the amplification process. In this setup, an 80 cm long Yb-doped photonic crystal fiber rod is employed, which is back-pumped by a continuous wave pump diode operating at a wavelength of 976 nm with a power of 250 W. The frequency comb is equipped with an in-built stretcher that minimizes
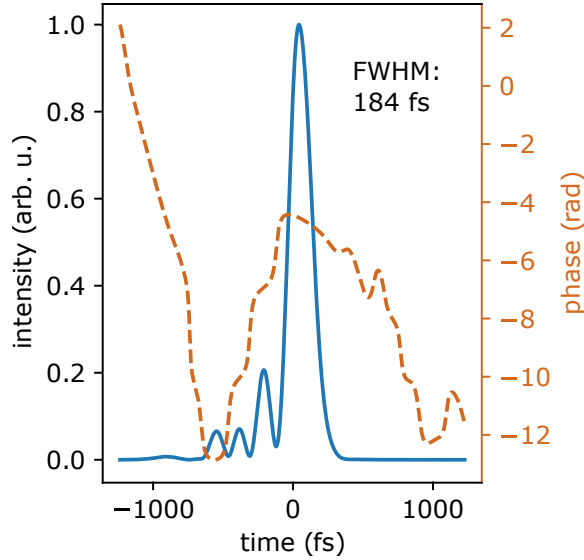
Figure 3.2: The temporal pulse shape and temporal phase of the laser pulses as measured using a FROG setup. Figure from [16].

the peak power and prevents overpowering the amplifier. Additionally, a Faraday isolator is employed to protect the frequency comb laser from any harmful back-reflections. This setup has the capability of amplifying the initial seed signal up to 90 W. Finally, a grating compressor is utilized to shorten the pulse duration of pulses exiting the rod-type fiber. The transmission grating used has a density of 1000 lines mm^{-1} and is positioned between two retro-reflectors. This arrangement compresses the pulses to a duration of ~ 185 fs, as shown by the frequency-resolved optical gating (FROG) measurement in Figure 3.2.

The laser system, which includes the frequency comb oscillator, fiber amplifier, and compressor, has good pointing stability. Only minor adjustments to the seed and pump light coupling into the high-power fiber amplifier are required, typically every few weeks at most. One significant advantage of the fiber-based high-power amplifier is that it serves as an excellent beam reference and isolates the components of the laser system. Even if the coupling into the amplifier fiber is disrupted, the beam path beyond the fiber remains aligned [7, 16].

The grating compressor integrated into the fiber amplifier effectively compensates for dispersion, allowing for nearly complete dispersion compensation. Essentially, almost bandwidth-limited pulses are obtained after the compressor. A bandwidth-limited pulse, also known as a transform-limited pulse, is a pulse of light that has the shortest possible duration allowed by its spectral bandwidth. In other words, it is a pulse that is limited in duration by the uncertainty principle in the frequency domain, as described by the Fourier transform.

Since the duration of a pulse is inversely proportional to its spectral bandwidth according to the uncertainty principle, it is imperative to increase the spectral content of the pulse in order to decrease the pulse duration. To make a Fourier-limited pulse shorter, one can employ techniques that increase the pulse's spectral bandwidth, resulting in a shorter pulse duration. A Fourier-limited pulse has a well-defined frequency spectrum, with all the frequency components perfectly synchronized.

To achieve effective nonlinear spectral broadening by SPM, it is crucial to accumulate substantial nonlinear phase. The utilization of a material with a high nonlinear refractive index n_2 proves advantageous in this regard. It is also necessary to maintain a high-intensity level for a specific propagation distance. However, the high repetition rate of 100 MHz, coupled with a pulse energy of approximately 0.75 μJ, results in a considerable average power of 75 W. Assuming an input of 185 fs pulses at the compressor, the peak power would be approximately 4 MW which falls within the critical power range of commonly utilized materials like FS. Consequently, the design of the pulse compressor must take into account these constraints.

3.2 Spectral broadening in multi-pass geometry

The so far most commonly used MPC geometry [45] consists of the Herriott-type configuration with two identical concave mirrors, as shown in Figure 2.4. However, convex-concave configurations can also be realized and are characterized by large mode volume [56]. Similar to an optical cavity, a Herriott cell forms transverse eigenmodes and preserves the Gaussian beam q-parameter of a beam mode matched to the MPC eigenmode. This means that the incoming beam only remains confined in the cell for multiple reflections if the same stability criterion as for optical cavities is fulfilled.
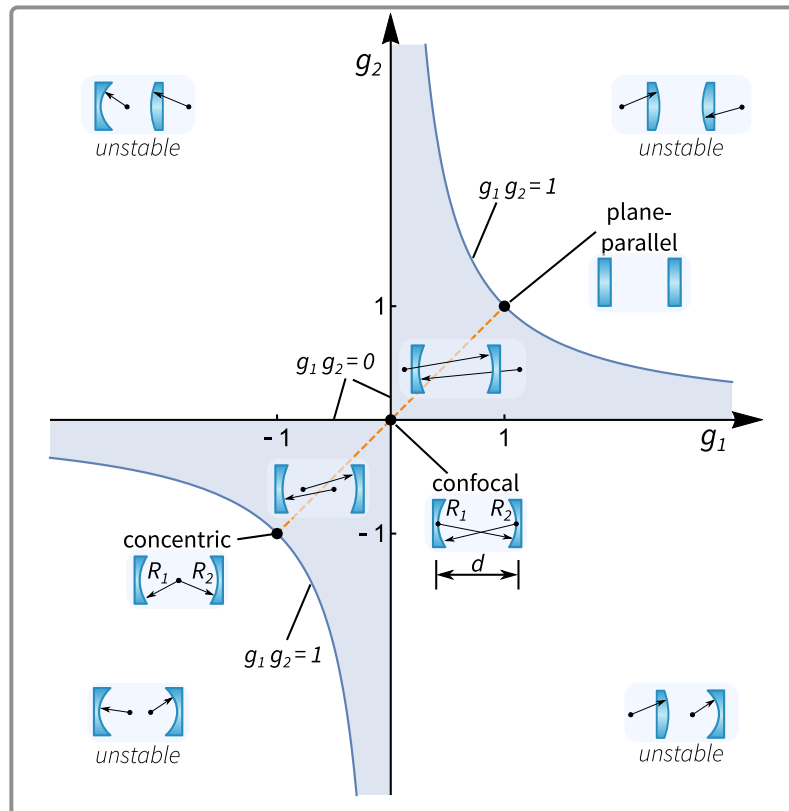
Figure 3.3: Stability diagram for laser cavities. The colored region is the stability zone which can be defined as the range of focusing mirror distances where the stability criterion (Equation 3.1) is fulfilled. Symmetrical resonators are located on the orange diagonal line. MPCs are operated close to the stability edge in the concentric geometry. Figure from [16].

Different optical cavity types are distinguished by the focal lengths of the two mirrors and the distance between them. The geometry (cavity type) must be chosen so that the beam remains stable, i.e. the size of the beam does not continually grow with multiple reflections. For a resonator with two mirrors with radii of curvature R_1 and R_2, there are a number of common cavity configurations. If the two radii are equal to half the cavity length L ($R_1 = R_2 = L/2$), a concentric or spherical resonator results. This type of cavity produces a narrow beam waist in the center of the cavity, with large beam diameters at the mirrors. Only certain ranges of values for R_1, R_2, and L produce stable cavities in which periodic refocusing of the intra-cavity beam is produced. The stability criterion is

$$0 \leqslant \left(1 - \frac{L}{R_1}\right)\left(1 - \frac{L}{R_2}\right) \leqslant 1. \tag{3.1}$$

Values that satisfy the inequality correspond to stable resonators. The stability can be shown graphically by defining a stability parameter, g for each mirror

$$g_1 = 1 - \frac{L}{R_1}, \quad g_2 = 1 - \frac{L}{R_2}. \tag{3.2}$$

Areas bounded by the line $g_1 g_2 = 1$ and the axes are stable, as seen in Figure 3.3. After one round trip, the spot on the mirror advances an angle φ. For a q-preserving cell where the beam is coupled out after n round trips

$$n\varphi = m\pi. \tag{3.3}$$

The ABCD matrix formalism can be used to better understand the back-and-forth propagation of the beam in the MPC. A ray-transfer ABCD matrix of an optical system relates the output ray (with position y_{out} and angle θ_{out}) to the input (with position y_{in} and angle θ_{in}) according to

$$\begin{bmatrix} y_{\text{out}} \\ \theta_{\text{out}} \end{bmatrix} = \begin{bmatrix} A & B \\ C & D \end{bmatrix} \cdot \begin{bmatrix} y_{\text{in}} \\ \theta_{\text{in}} \end{bmatrix}. \tag{3.4}$$

For the case when the beam propagates through several optical elements, a single matrix M_{tot} is used.

$$M_{\text{tot}} = \begin{bmatrix} A & B \\ C & D \end{bmatrix}. \tag{3.5}$$

M_{tot} is the product of all the single matrices of each of the k optical elements

$$M_{\text{tot}} = M_k M_{k-1} ... M_1. \tag{3.6}$$

The ray transfer matrix for one round trip across the MPC with mirrors having identical radii of curvature R can be written as

$$M_{\text{MPC}} = \begin{bmatrix} 1 - \frac{2L}{R} & 2L\left(1 - \frac{L}{R}\right) \\ -\frac{2}{R} & 1 - \frac{2L}{R} \end{bmatrix}. \tag{3.7}$$

where $\cos\varphi = 1 - 2L/R$. The MPC configuration can be unfolded into a series of thin lenses of focal length $f = R/2$, each separated by a length of equal distance L to represent an equivalent resonator [57]. By varying L, possible values of φ that satisfy Equation 3.3 can be found. Figure 3.4 shows the spot pattern for 11 round trips.
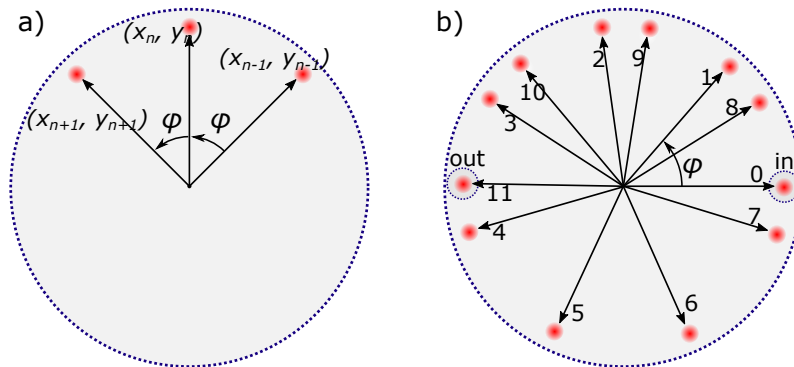
Figure 3.4: The spot pattern on the curved mirrors. a) Consecutive spots advance by an angle φ on the curved mirrors. b) The spot pattern for 22 passes on the first curved mirror is shown. This corresponds to $m = 3$, $n = 11$ and $\varphi = 49.1°$. Small dotted circles representing scraper mirrors indicate in- and out-coupling positions. The in-coupled spot is labeled spot number 0 and the reflected light passes through the nonlinear medium and bounces back from the second curved mirror to pass the nonlinear medium again and gets reflected from the first curved mirror at spot number 1. Figure from [16].

As the Gaussian beam propagates through the MPC, the q-parameter is transformed to

$$q' = \frac{(Aq + B)}{(Cq + D)}. \tag{3.8}$$

After each round trip, $q' = q$. Hence,

$$q' = -\frac{R}{2}\sqrt{\frac{L}{R}\left(\frac{L}{R} - 2\right)} \tag{3.9}$$

The q-parameter provides full information about the spot size and curvature. The focal spot radius ω_0 and the spot radius at the mirror position ω_m for a fundamental Gaussian mode can be calculated as

$$\omega_0^2 = \frac{R\lambda}{2\pi}\sqrt{\frac{L}{R}\left(2 - \frac{L}{R}\right)}, \tag{3.10}$$

$$\omega_m^2 = \frac{R\lambda}{\pi}\sqrt{\frac{\frac{L}{R}}{2 - \frac{L}{R}}}. \tag{3.11}$$

3.2.1 Parameters

In this section, we discuss a few basic steps to consider when setting up an MPC for pulse compression. We concentrate on the case of symmetric Herriott-type MPCs (two concave mirrors in a near-concentric configuration) with circular beam patterns to reach bandwidths supporting pulse duration of a few tens of femtoseconds.

i. Nonlinear medium

The selection of the nonlinear medium, whether it be gas or bulk plates, is usually determined by considering the input peak power of the cell and the desired spectral broadening ratio. Solid-state crystals exhibit nonlinearities approximately three orders of magnitude greater than those observed in gases [44]. Thus, for our experiment, we choose to use a bulk material. Even if the MPC hosts a tight focal spot, the bulk nonlinear material can be placed at a location of lower intensity. B-factor per pass depends on the length of the material (Equation 2.19). However, at high powers, Kerr-lensing causes bulk material damage if the physical material length exceeds the critical self-focusing length. Therefore, the nonlinear propagation length is restrained, and the attainable spectral broadening factors are comparably low. The multi-plate approach [58] proves to be successful in such a case. Multiple plates of the nonlinear medium can be stacked close together, for periodic re-focusing in the plate and diffraction outside the plate, allowing to scale in power without disrupting the pulse. We choose the two and three-plate approach with 6.35 mm thick FS plates (141935, Layertec).

ii. Mirror curvature

The MPC mirror curvature determines the maximum length of the MPC setup due to the near-concentric regime it is operated in. The selection of the value is typically made to ensure that the mirror fluences and focus peak intensities remain sufficiently low, thereby avoiding damage and ionization. For our experiment, both curved mirrors have a radius of curvature of -250 mm (025-8025, EKSMA Optics). This choice strikes a good balance between system compactness ($L \approx 500$ mm) and a sufficiently large focal length to avoid alignment difficulties and instabilities.

iii. Size of curved mirrors

The size of the MPC mirrors is determined by the number of passes employed for compression, as it establishes the maximum separation between adjacent spots in the circular multi-pass pattern. It is essential to have an adequate distance to minimize losses during in- and out-coupling. Interestingly, instead of MPC mirrors, individual small mirrors can also be used for each beam reflection [59]. In our case, the curved mirrors have a diameter of 50.8 mm.

iv. Distance between curved mirrors

The upper limit of the distance between the two concave mirrors is defined by their radii of curvature, as described by the stability criterion in Equation 3.1. In accordance with the cavity-like behavior of the in-coupled beam, the beam retraces itself only below the stability edge. This property also defines the spot size of each reflection on the mirrors (Equation 3.10). The larger spot size at the mirrors, for a given diameter of the two curved mirrors, although corresponds to a narrow waist at the MPC center, makes the inter-spot distance less. This causes problems to out-couple the desired last spot as it may overlap with the second last spot.
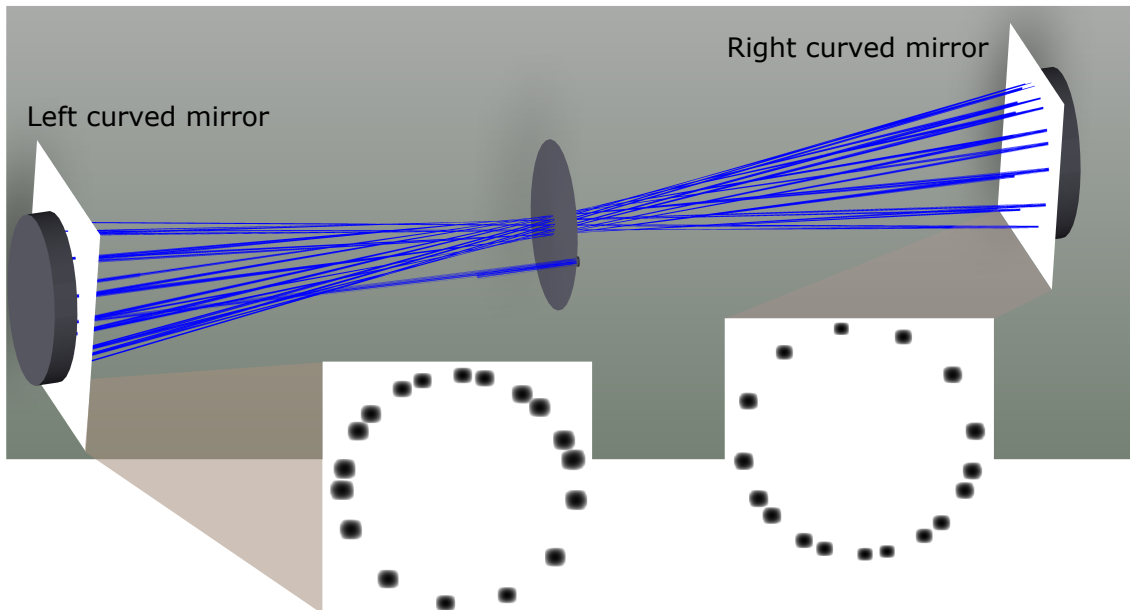
Figure 3.5: MPC assembly simulated using Zemax OpticStudio. The two curved mirrors have a distance of 489 mm. The beam goes back and forth 34 times. Two detector surfaces (white rectangles) are positioned in front of the mirrors to image the spot pattern shown in the insets.

To better analyze the geometry, the MPC setup was simulated using Zemax OpticStudio. This software provides a platform to model optics. A key parameter in the alignment of the MPC is the distance between the big curved mirrors. It was found using OpticStudio that for a given radius of curvature of the big curved mirrors, the number of spots per circle in the Herriott configuration depends on the distance between the two mirrors. To get 34 passes, the mirrors can be placed 489 mm apart, as shown in Figure 3.5. Another factor to keep in mind is the proper out-coupling of the beam as it is felicitated by a scraper mirror which needs to be positioned right opposite the first scraper mirror.

Given these interdependencies, it is, first, realized that the waist at the center of the cell needs to be so that we have enough non-linear effects generated in the bulk medium but that does not result in peak powers above the critical power for self-focusing. Second, we can only couple out the beam after 0.5 or 1.5 complete rounds of the spot pattern, due to the position of the second scraper mirror. 2.5 or 3.5 rounds are not possible because we are limited by the number of spots that can be accommodated on the mirrors due to their finite size and the closer the spots are, the harder it becomes to couple the last one out without clipping the neighboring spots. This puts a limit to the number of passes through the bulk medium possible with the MPC. Fortunately, in accordance with the performed simulations, we still have a wide range of parameters to operate the cell.

For the compression ratios we are interested in, a beam waist of $\sim 100\,\mu m$ is sufficient to incorporate enough nonlinear effects without damaging the FS plates. So, we mode matched to a waist of $\sim 95\,\mu m$ for a distance of $\sim 495\,mm$ between the big curved mirrors. For this distance between the curved mirrors, we coupled out the beam after 1.5 rounds, giving us 34 passes through the fused silica plates. The 17th spot was coupled out by the second scraper mirror.
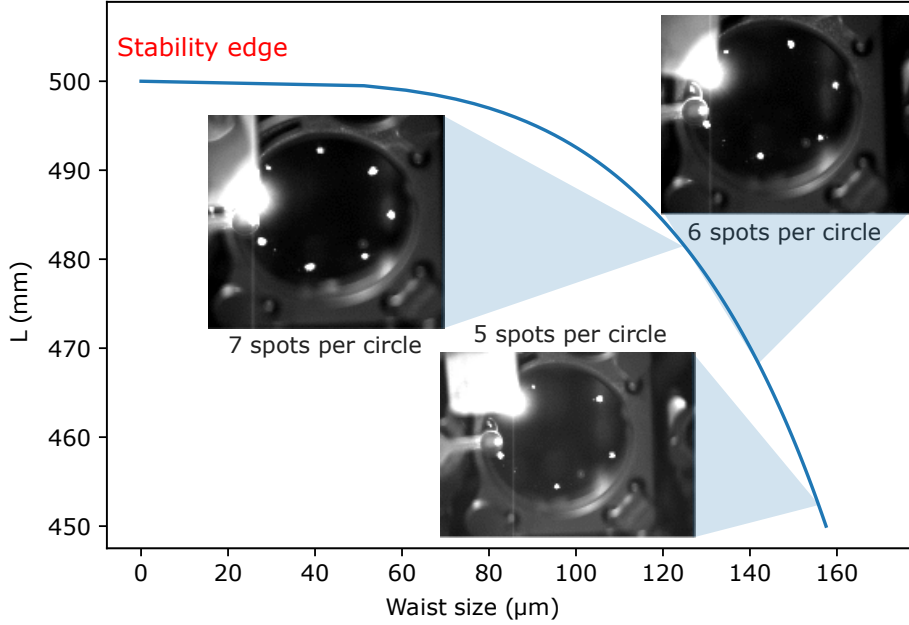
Figure 3.6: Evolution of the number of spots per circle for a fixed size of the curved mirrors as a function of the distance between two mirrors. The corresponding waist at the center of the MPC is plotted on the x-axis. Insets show the number of spots per circle on the first curved mirror. The 0th spot at the in-coupling scraper mirror is not counted. The second circle is blocked using a detector card.

v. Number of spots per circle

For a given diameter of the mirrors, the number of spots per circle reduces with a reduced inter-mirror distance (Figure 3.6). Hence this acts as a constraint on the possible number of passes through the MPC center because with a fixed position of the scraper mirrors, the last spot must couple out after an angular advance of $m\pi$ (Equation 3.3). Here, m gives the number of semicircular arcs that the bouncing beam traverses on one of the mirrors before the q-parameter is transformed back to its initial value.

3.2.2 Design and construction

The MPC is a novel addition to the pre-existing experiment involving the XUV-frequency comb [7, 16]. To incorporate shorter pulses in the experiment, a mirror is set up on a magnetic mount to send the laser toward the MPC setup. The beam height is adjusted using a periscope which directs the laser and elevates the height from 81 mm to 123.3 mm.

A system of three lenses is designed to mode-match the in-coupled beam to the MPC. The out-coupled beam is diverging, so a system of two lenses is set up to collimate the beam. A heightened breadboard [60] is designed for the stability of the assembly, as shown in Figure 3.7. The lenses are mounted on 250 mm long rails, allowing fine-tuning of the lens positions. The lens mounts (ST1XY-A/M, Thorlabs) offer $\pm\,3\,$mm of XY translation.

The MPC design is one of its kind as it enables the use of bulk media and inert gases in the same cell for pulse broadening [16, 30]. The primary optical elements- the big curved mirrors, the crystal mount, and the in- and out-coupling mirrors- are positioned on a
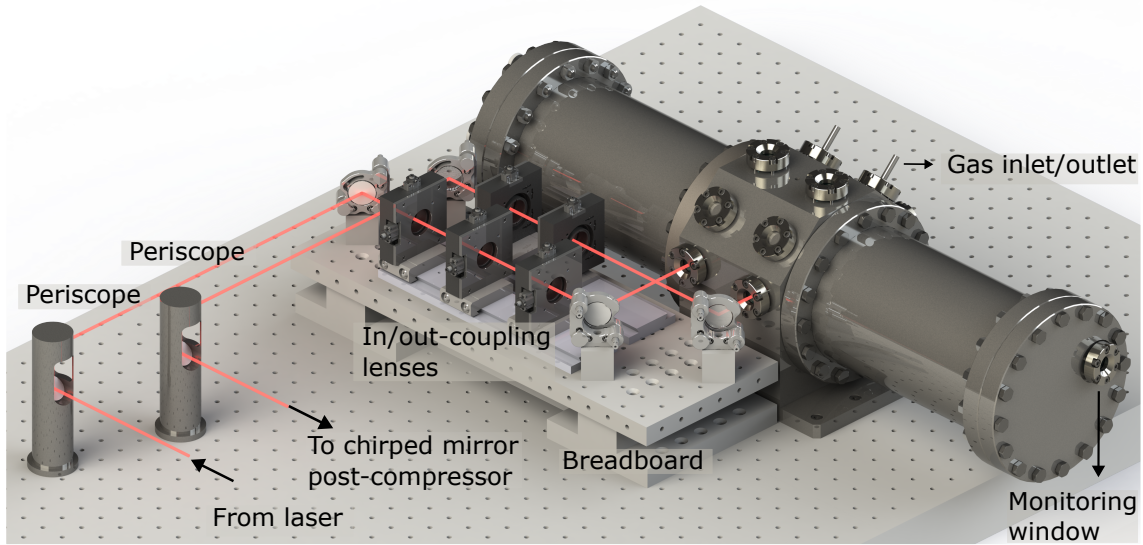
Figure 3.7: Design of the in- and out-coupling assembly with focusing and collimating lenses mounted on rails. The laser is first guided by a periscope from 81 mm to 123.3 mm height. Then it is converged to mode-match to the MPC. The out-coupled beam is then collimated at brought back by another periscope to 81 mm beam height to be sent to the enhancement cavity.

sturdy 630 mm stainless-steel mounting structure with a U-shaped cross-section, as shown in Figure 3.8 ii). This structure is securely held in place by a water-cooled main framework (referred to as the hexablock, because of its hexagon shape) that is connected to the optical table which has a height of 180 mm and a footprint of $130 \times 175 \, mm^2$.

The laser pulses enter the cell by passing through a $\varnothing$ 25 mm anti-reflective coated FS window. Subsequently, they are reflected by a 45°, $\varnothing$ 12.7 mm high reflection (HR) mirror, which is mounted on a 2-axis kinematic mount (Polaris-K05, Thorlabs). The reflected pulses are directed towards the $\varnothing$ 6.35 mm high-reflectivity scraper mirror (Layertec) positioned at 0°. The scraper mirrors are glued to 5.5 mm wide aluminum arms, which can be adjusted in terms of length and angle. They are held in place by kinematic mounts (Polaris-K05, Thorlabs) that allow for two-axis tilting and shifting along the beam propagation direction. The two curved mirrors themselves are secured in 2-axis kinematic mounts (POLARIS-K50S4/M, Thorlabs).

At the center of the cell lies the nonlinear crystal, which is situated in a rotatable holder within the crystal mount. This arrangement enables adjustments to the crystal's position concerning the fixed laser beam pattern, especially in cases of spot burn-in. To enhance heat conductivity, the crystal holder is crafted from annealed copper. Additionally, stainless steel components such as screws, thread inserts, and a ring are employed to ensure an even distribution of clamping pressure.

Since all these optics are subjected to high laser powers, it is important to take suitable measures for heat dissipation to avoid damage and unstable beam pointing. Copper braids measuring $2 \, mm^2$ are welded to copper end fittings, forming flexible links that thermally connect the curved and scraper mirrors (as can be seen in Figure 3.9), as well as the crystal mount, to the main structure, even under vacuum conditions. The hexablock itself is water-cooled by a serpentine-like water-cooling channel (Figure 3.8 iii)), 20 mm deep and
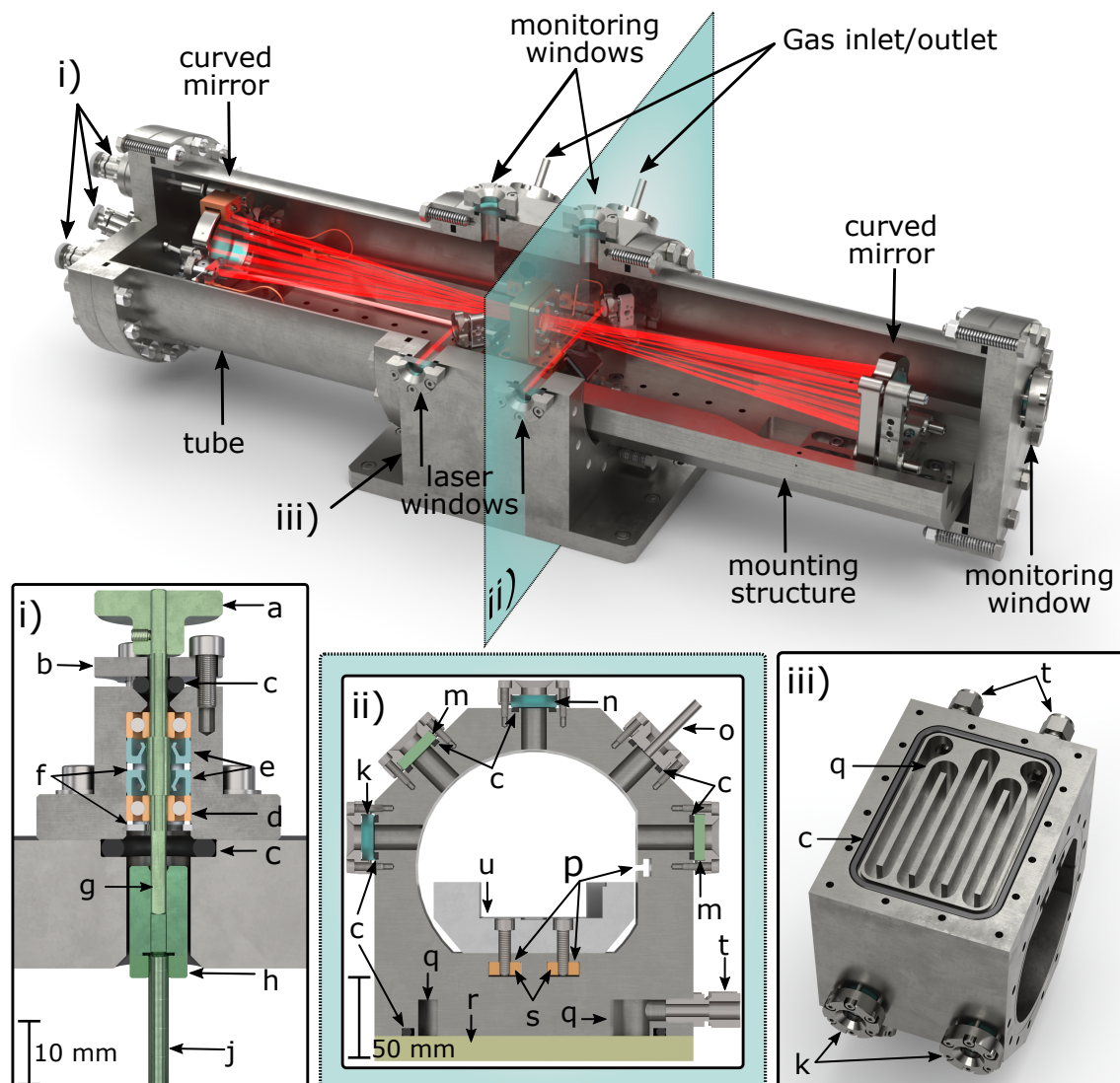
Figure 3.8: Sectional view of the MPC. Laser is in- and out-coupled through windows. Access to optics during closed-cell operation is provided by i) the rotary feedthroughs with a: knob, b: endcap, c: O-rings, d: ball bearings, e: radial shaft seals, f: spacer, g: shaft, h: shaft coupler, and j: flexible shaft. ii) Cross-sectional view of the hexablock with the optics mounting structure depicts the slot nuts (s) inserted into T-slots (p). The other components are k: AR-coated laser window, m: blind flange, n: monitoring window, o: gas inlet/outlet, q: water channel, r: baseplate, t: cooling water connection, and u: optics mounting structure. iii) Design of the cooling channels at the bottom of the hexablock without the baseplate screwed in. Figure adapted from [16].
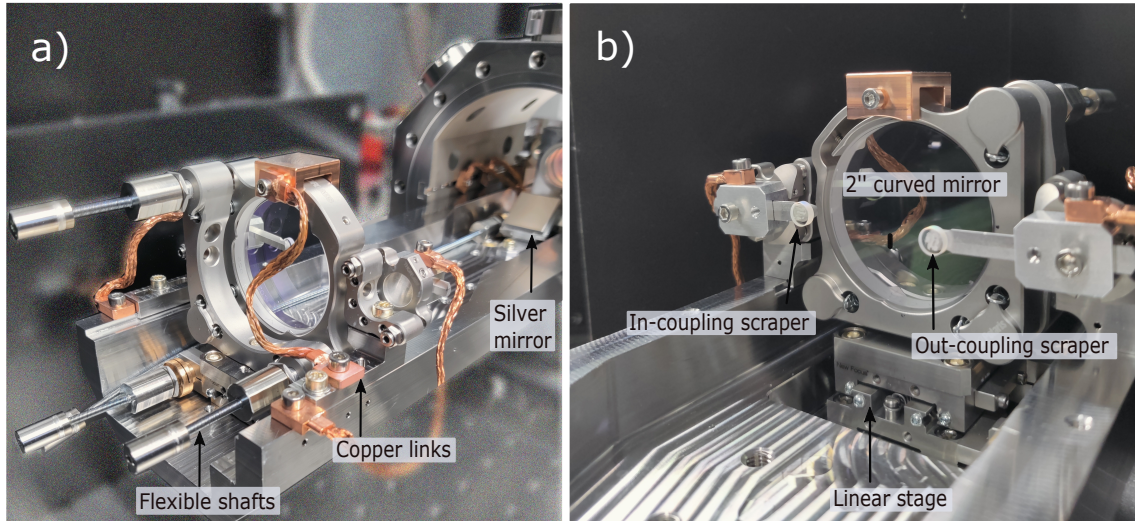
Figure 3.9: The left curved mirror as looked from the a) back and b) front. The mirror is mounted on a linear stage for fine adjustment of the cell length. Copper braids connect the mirror mounts to the optics mounting structure for heat dissipation. Flexible shafts connect the mirror to the rotary feedthroughs for accessibility during closed-cell operation.

6.75 mm wide, from the bottom. Cooling water is supplied through $1/4''$ NPT screw-in connections with 10 mm double ferrule tube fittings. A 14.5 mm thick base plate measuring $175 \times 225\,\mathrm{mm}^2$ mounts the hexablock and in turn the entire cell on the optical table.

Two angled silver mirrors are positioned on the U-shaped mounting structure. They enable viewing the spot patterns on each of the curved mirrors and scraper mirrors during alignment and operation. This can be done through a top window flange in the hexablock as shown in Figure 3.10. Another window flange on the side of the right curved mirror enables viewing the nonlinear crystal/crystals. As described before, the spot pattern is sensitive to the distance between two curved mirrors, and for fine-tuning this, the left curved mirror is placed on a translation stage (custom UHV version of 9062-COM-M, Newport). This stage can further be positioned in relative configurations of 0 mm, 8 mm, and 16 mm. It can be accessed through a flexible shaft (100881, Gemo) via feedthroughs under closed-MPC operation. The right curved mirror is also mounted on a home-built stage. For optimizing the crystal position with respect to the cell center along the z-axis, the same combination of a translation stage and flexible shaft used for the curved mirror is employed to move the crystal mount.

To form a gas-tight chamber, tubes with a length of 255 mm (including flanges) and an inner diameter of 130 mm are attached to both sides of the main structure. The advantage of this mounting structure is that any pressure-induced changes in dimension do not affect the alignment of the optics, as it is mounted on the hexablock via T-slots and secured with M6 screws.

The main structure features ten access ports with DN16CF-inspired flanges. These flanges have the same inner bore diameter and screw pattern as DN16CF flanges but use an FKM O-ring instead of copper gaskets for sealing. The O-ring is placed in a groove to prevent it from expanding or shrinking, ensuring a tight seal under both vacuum and overpressure conditions. These access ports are used for various purposes such as installing AR-coated
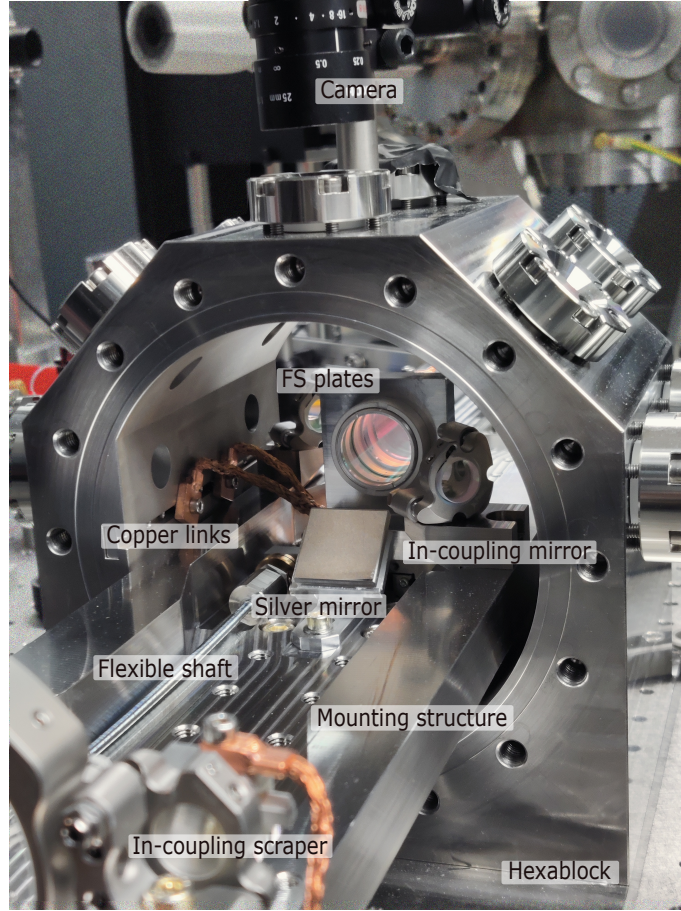
Figure 3.10: Image of the hexablock which mounts the U-shaped mounting structure on which all the optics are mounted. The left curved mirror is viewed using a camera through a window-flange on the hexablock. FS plates are stacked in a stainless steel mount.

laser windows, uncoated windows for monitoring the mirrors with an airside camera, gas injection, and pumping.

A lot of attention to detail has been paid to the mechanical design of the cell [16, 30]. One of the highlights is the flange (Figure 3.8 i)) with rotary feedthroughs provides access to a few selected optics inside the cell when it is closed. On the atmospheric side, a removable knurled knob is affixed using an inset screw. Inside the MPC, the rotating shaft connects to a flexible shaft via a coupler. These rotary feedthroughs are designed to withstand both over-pressure and under-pressure conditions.

3.2.3 Scaling limits

We now address the question of the energy-scaling limits of the MPC. Multiple limitations can be taken into account, like the optical damage on the MPC mirrors, the nonlinear bulk medium, and their coatings, defined by the laser-induced damage threshold quantified by fluence F_m [46]

$$F_m = \frac{2E_p}{R\lambda}\sqrt{\frac{2 - L/R}{L/R}} \tag{3.12}$$
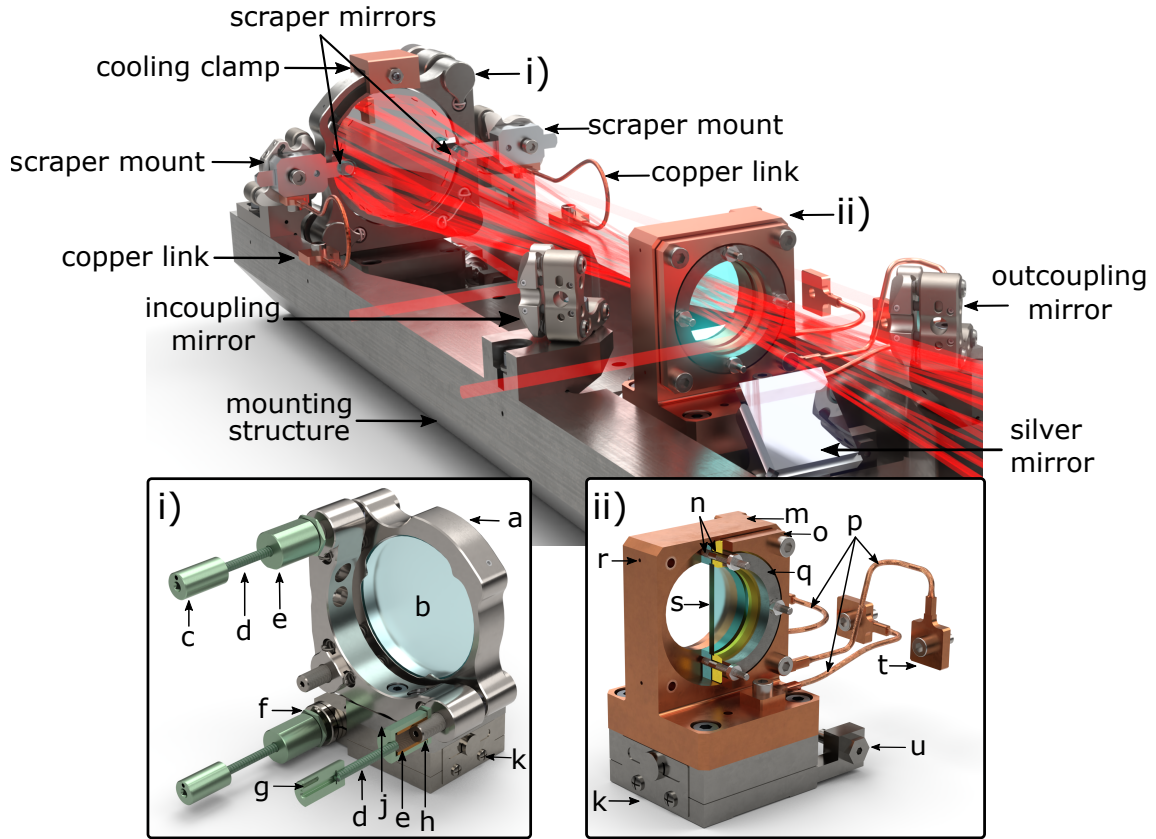
Figure 3.11: Detailed view of the optics inside the MPC. The rigid mounting structure and mirror mounts are made from stainless steel. Inset i) shows the left curved mirror with a: mirror mount, b: ⌀ 50.8 mm mirror, c: shaft coupler, d: flexible shaft, e: actuator adapter, f: locking nut, g: thread for threaded rod, h: actuator of mirror mount, j: adapter plate, and k: translation stage. Inset ii) shows the rotatable crystal holder made from copper in detail: m: mount, n: crystal holder plates, o: holding plate, p: flexible copper links, q: steel ring, r: degassing hole, s: crystal, t: copper link connection, u: micrometer screw, and k: translation stage. Two silver mirrors, mounted at an angle, are used to image the curved mirrors with a camera (not shown) outside the chamber. Figure adapted from [16].

where E_p is the pulse energy. The onset of ionization in the gas medium is another limitation, defined by the focal peak intensity above which the ionization rate is too high to ensure proper operation of the MPC. This defines a maximum pressure for a particular gas used to fill the MPC, which puts a limit on the achievable B-integral per round trip [61]. But several experimental demonstrations approach this limit as it was observed that the spatio-spectral homogeneity remains satisfactory even for peak powers above half the critical power [62]. The nonlinear medium can be placed close to the concave mirrors maximizing its damage threshold [44].

When operating MPCs at high nonlinearity levels, a lower number of round trips are required for a given compression ratio which relaxes constraints on the mirror coatings in terms of reflectivity and dispersion. Hence, it is important to strike a balance between the aforementioned limits and the transmission of the cell.

3.2.4 Dispersion control

The MPC has been designed as a gas cell that can withstand pressures from a vacuum up to 6 bar of over-pressure. This is to use the dispersive property of inert gases at high pressures to fine-tune the dispersion in pulses, as can be seen in Figure 3.12 c).
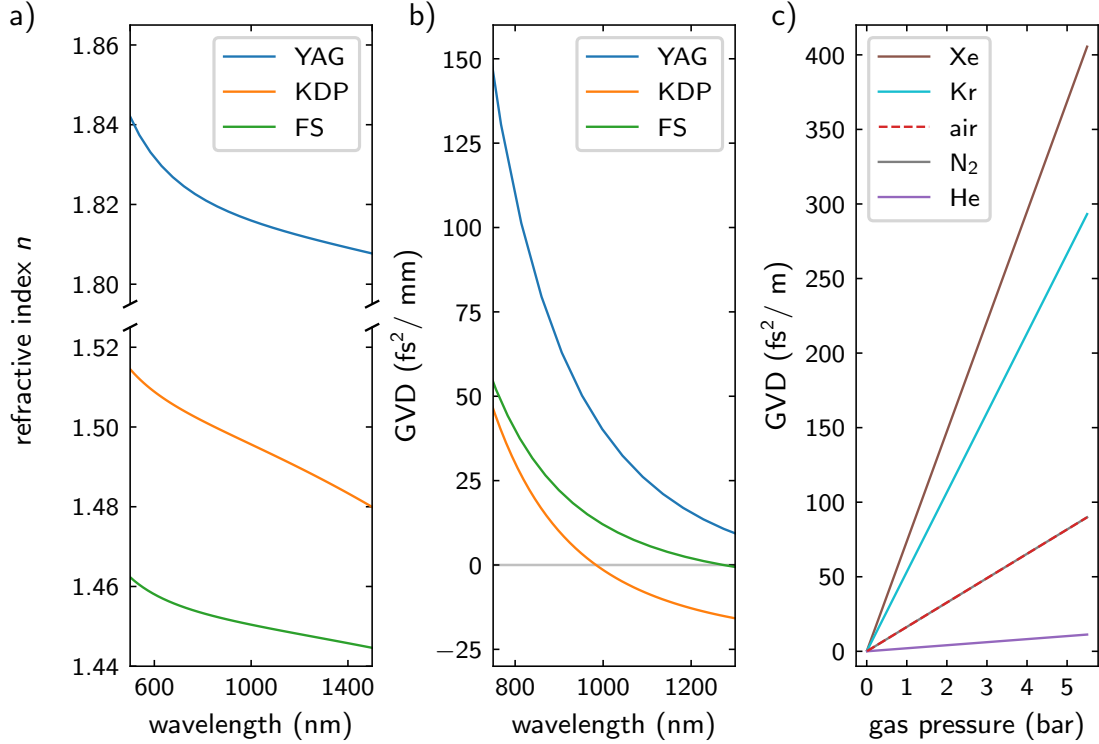
Figure 3.12: Positive dispersion from pressurized gases as a method to tune dispersion in the MPC. a) Wavelength dependency of refractive indices of YAG, KDP and FS. b) Dispersion values of these materials are obtained by the second derivative. c) The dispersion in the MPC can be tuned by changing the gas pressure. The GVD is plotted for selected gases. Note that the dispersion of air and nitrogen is almost identical. Figure from [16].

Pumping and gas injection in the cell is accomplished through flange-mounted inlets and outlets. To establish the connection, a flexible all-metal tube with an inner diameter of 6 mm links the cell to a gas panel. This flexible connection enables unrestricted movement of the floating optical table and reduces the transmission of vibrations. Figure 3.13 illustrates the gas panel, which facilitates cell pumping and inert gas filling. The pump outlet is connected to the fore-vacuum system of the XUV comb experiment, offering the advantage of recycling the gas used in the cell through the gas-recycling setup existing in the lab.

In the gas panel, a regulating and shut-off valve is incorporated for the continual pumping of the cell to reach the desired pressure. An additional advantage is that the cell pressure can be smoothly released without surpassing the maximum allowable pressure of the fore-vacuum line. The same valve is also positioned downstream of the pressure regulator (Swagelock KCY1FRF412A20000). Moreover, the gas panel is connected to the institute's nitrogen supply. A pressure relief valve with a release pressure of 8.5 bar is installed to
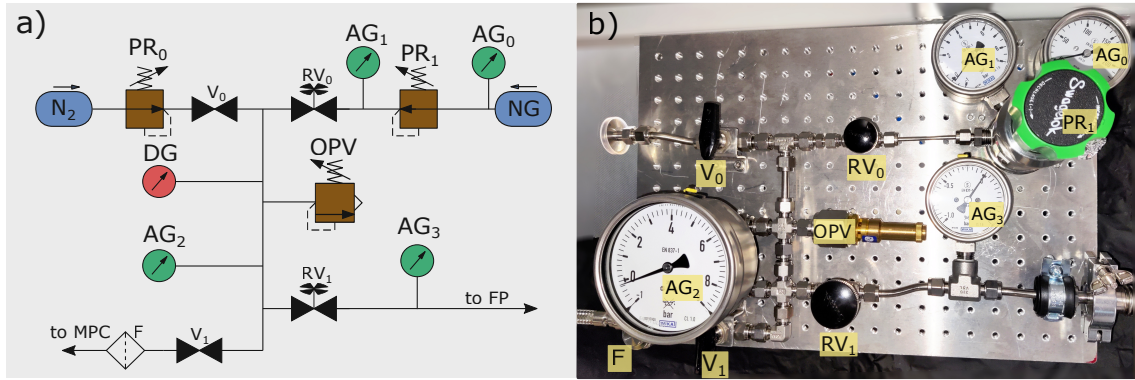
Figure 3.13: Circuit diagram a) and photograph b) of the MPC gas system. Components: valves (V), regulating and shutoff valves (RV), pressure regulator (PR), filter (F), analog/digital pressure gauges (AG/DG), over-pressure valve (OPV), neutral gas tank (NG), and fore-vacuum pump (FP).

prevent the cell pressure from reaching dangerous levels. In order to prevent contamination of the system with dust and particles, a particle filter with a pore size of 0.5 µm serves as the final component of the gas panel before the connection to the cell.

Multiple approaches can be taken to control dispersion. With an anomalous dispersive bulk material as the nonlinear medium for spectral broadening, the positive chirp can be compensated by the medium itself. In that case, the positive dispersion in an inert gas can be used to fine-tune dispersion in the cell. In the case of normal dispersive bulk material like FS, temporal compression can be performed using chirped mirrors either in the cell at every pass, or with a chirped mirror post-compressor outside the cell. These mirrors are specifically designed so that longer wavelengths experience larger group delay dispersion than shorter wavelengths, allowing the shorter wavelengths to "catch up" to the longer wavelengths.

A chirped mirror is constructed by depositing multiple stacks of dielectric coatings with two alternating refractive indices of gradually increasing layer thickness resulting in lower reflectivity of longer wavelengths for layers further from the surface, and vice versa. As a result, longer wavelength components within the ultrashort pulse bandwidth will penetrate deeper into the dielectric coating. The wavelength-dependent optical path length results in negative (anomalous) GDD. A single reflection from a chirped mirror results in a fixed GDD, therefore, additional negative GDD can be provided in proportion to the number of reflections. The number of reflections depends mainly on the beam angle of incidence, mirror separation, and beam diameter.

3.3 Pulse characterization

Photodiodes and oscilloscopes, with response times on the order of 200 femtoseconds do not exist. So, accurately measuring ultrashort pulse durations requires employing the "autocorrelation technique" which involves correlating the temporal pulse trace with itself.

In an autocorrelator, an ultra-short pulse train is split into two beams, and one part is delayed using a variable delay stage, as is depicted in Figure 3.14. Then, both beams are

focused in a second-harmonic generation (SHG) crystal in such as way that the harmonic occurs only when both pulses temporally overlap. That gives a signal proportional to $(E(t) + E(t - \tau))^2$. Only the beam propagating on the optical axis, proportional to the cross-product $E(t)E(t - \tau)$, is retained. This signal is then recorded by a slow detector, which measures

$$I_A(\tau) = \int_{-\infty}^{+\infty} |E(t)E(t - \tau)|^2 dt = \int_{-\infty}^{+\infty} I(t)I(t - \tau)dt \tag{3.13}$$

where $I_A(\tau)$ is exactly the intensity autocorrelation $A(\tau)$. Hence, recording the signal with respect to the delay enables determining the length of the pulse.
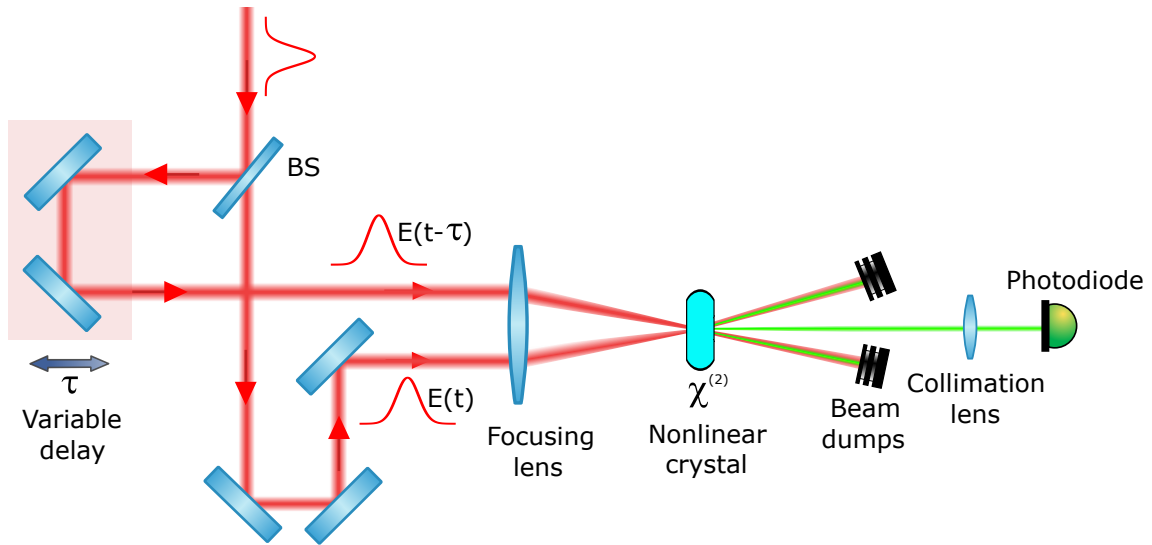
Figure 3.14: The setup for intensity autocorrelation involves splitting the beam into two parts, with one of them passing through an adjustable delay stage. Both beams are then focused into a nonlinear crystal. The response of the χ_2 crystal on the delayed pulses is subsequently measured using a photodiode.

A more advanced method that is also sensitive to chirps is the interferometric autocorrelation method. The pulses are collinearly focused into the nonlinear crystal forming an interference pattern and allowing correlation measurement of the electric field itself.

Another method is known as FROG in which in addition to the SHG signal, the spectral information is also measured for every delay step. Hence it enables complete pulse characterization.

4 Results

Significant observations were made during the systematic alignment and operation of the MPC. Concerning the Herriott-type cell geometry, the shape, and size of the spots on the curved mirrors proved to be key indicators of the accuracy in alignment. The more circular the spot pattern is, the better the mode matching of each individual pass. Furthermore, self-focusing of the beam inside the nonlinear medium at high laser powers changes the mode and must be accounted for.

The setup for pulse duration measurements is shown in Figure 4.1. The in-coupled laser power is measured with a reflection from a beam sampler after the mode-matching lenses. The out-coupled power is measured after the chirped-mirror compressor system. The power transmission through the cell after 34 passes in air and without any nonlinear medium is $\sim 85\%$.
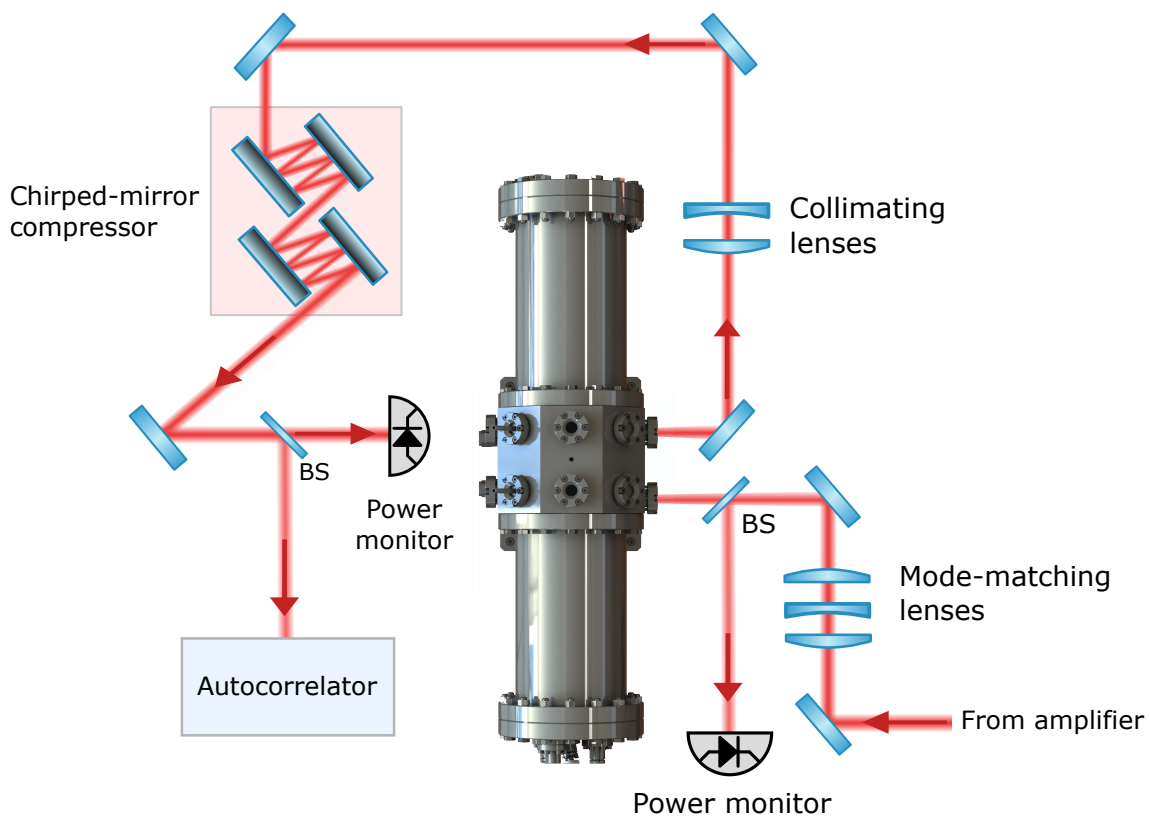
**Figure 4.1:** Schematic overview of the MPC optical setup for pulse duration measurements. The input beam from the amplifier is first mode-matched and then in-coupled via a window in the MPC. The out-coupled beam is collimated by a system of lenses and further post-compressed by a chirped-mirror compressor before finally being sent for out-coupled power monitoring and intensity autocorrelation.

4.1 Self-compression with KDP
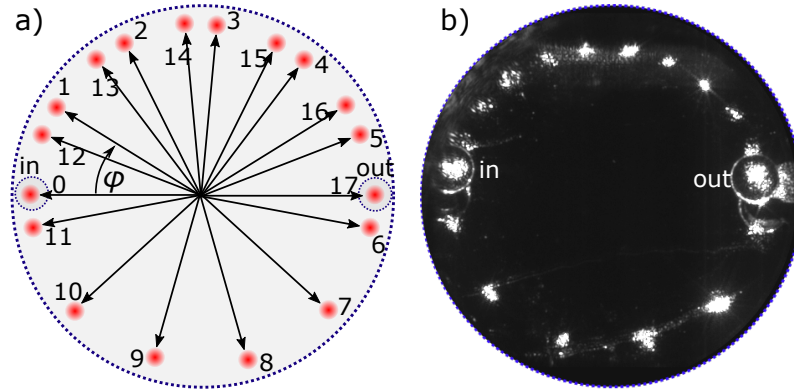
Figure 4.2: Spot pattern on the first curved mirror of the MPC for 34 passes which a) correspond to $m = 3$, $n = 17$, and $\varphi \approx 32°$. b) First curved mirror as viewed from a camera for 34 passes through KDP. Figure from [16].

The cell was assembled with a KDP crystal measuring $25 \times 25 \times 4 \, \text{mm}^3$. The configuration involved setting the number of passes to 34, as depicted in Figure 4.2. According to the simulation results, as shown in Figure 2.5, spectral broadening and pulse compression to approximately 40 fs was anticipated. Remarkably, this was expected to be achieved without the need for chirped cell mirrors or post-compression techniques. However, during the testing process, a significant issue arose. The crystal exhibited cracks when the input laser power rose to about 2 W (Figure 4.3 b)). According to the manufacturer (EKSMA Optics), the laser damage threshold for the crystal is $100 \, \text{GW/cm}^2$ for 1.06 μm wavelength and 10 ps long pulses. Surprisingly, a similar cracking occurred in another crystal from the same batch, which had a thickness of 3 mm (Figure 4.3 a)). It's worth noting that both crystals were meticulously mounted to minimize any mechanical stress caused by the holder. To investigate the root cause of the crystal breakdown, a thermal camera (E6xt,
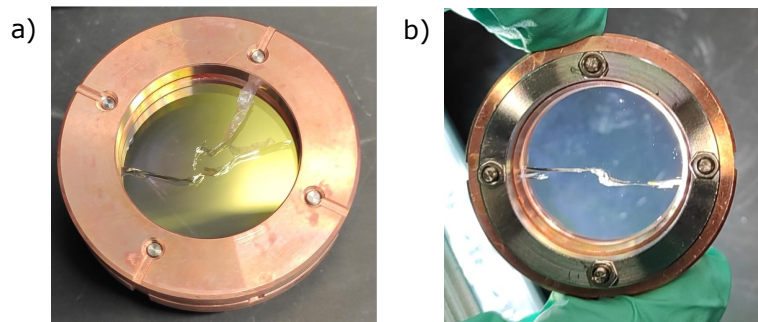
Figure 4.3: Photographs of KDP crystals of thickness a) 3 mm and b) 4 mm damaged at $\sim 2 \, \text{W}$ input power.

FLIR) was utilized to monitor a fragment of the 4 mm thick crystal during a 5-pass run. At approximately 2 W of optical power, the crystal quickly reached a temperature of 44 °C and broke. In a previous experiment, a KDP crystal from a different manufacturer, in a single-pass, uncooled configuration, was tested with power levels of around 73 W without experiencing any damage. Notably, spectral broadening induced by SPM was observed in that experiment [30].

Based on these observations, the most probable explanation for the former mentioned crystals' failure is a defective crystal batch from the manufacturer. Unfortunately, large KDP crystals of this nature are not readily available and often have long lead times, exacerbating the challenge of finding a suitable replacement. Therefore, the measurements were carried out with more readily available FS crystals.

4.2 Multi-plate approach with fused silica

As described before, a multi-plate approach can be followed to avoid disruptive self-focusing in the nonlinear medium, particularly when dealing with extensive medium lengths. We measured the spectral broadening of our pulses with a two and three-plate setup, as shown in Figure 4.4. Each plate is 6.35 mm thick and 25 mm in diameter. The spot pattern in the crystal is about 10 mm wide.
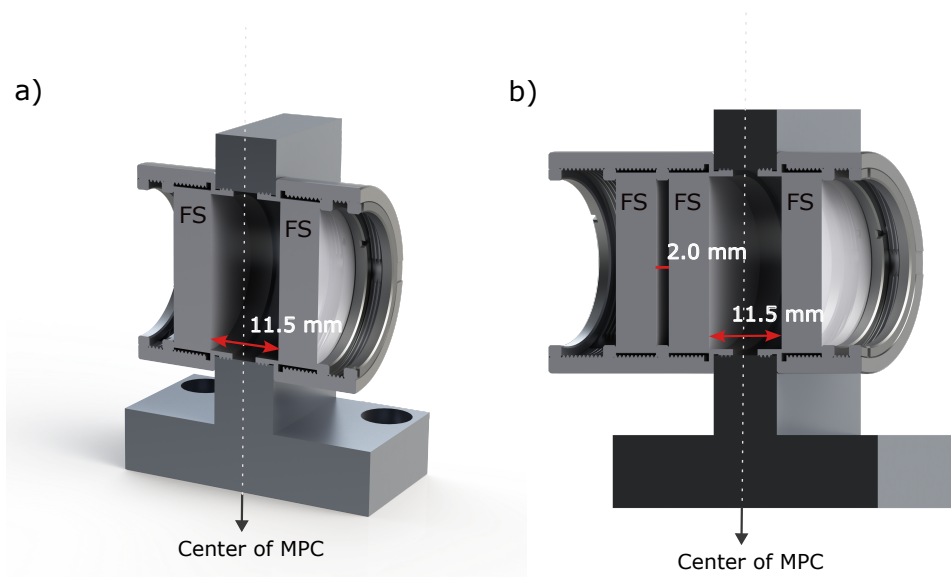

Figure 4.4: a) Two and b) Three plate assembly of FS plates mounted on a T-shaped holder.

Two-plate assembly with FS

The spot pattern for 34 passes through two plates of FS mounted as shown in Figure 4.4 can be seen in Figure 4.5. And the in- and out-coupled beam profiles are shown in Figure 4.6. The power transmission through the cell is $\sim 81\%$ with two FS plates and $\sim 74\%$ with three FS plates. The transmission is limited by the HR coating of the curved mirrors, the anti-reflection (AR) coating of the in- and out-coupling windows of the MPC, and the AR coating and the transmission of the FS plates.

To measure the spectral content of our pulses, we use a spectrometer (Qmini NIR, BROAD-COM). The spectrum measurements are carried out after the collimating lenses shown in Figure 4.1. A home-built integration sphere is used to couple light to the spectrometer using

a multi-mode fiber. Spectral broadening due to SPM can be confirmed by the emergence of spectral wings at high powers, as shown in Figure 4.7. The broadening is asymmetric and can be due to the presence of a pre-pulse in the input pulse, as shown in Figure 3.2.
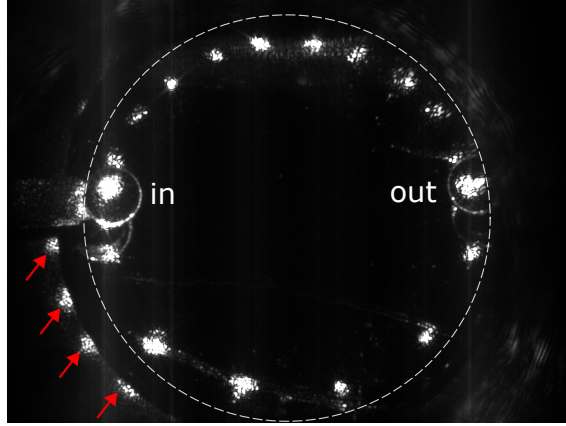

Figure 4.5: First curved mirror as viewed from a camera. The spot pattern corresponds to 34 passes through two plates of FS. The in- and out-coupled spots are labeled and, the dashed circle is marked to showcase the circular geometry of the pattern. The red arrows point towards some back-reflections from the FS plates hitting the mirror mount.
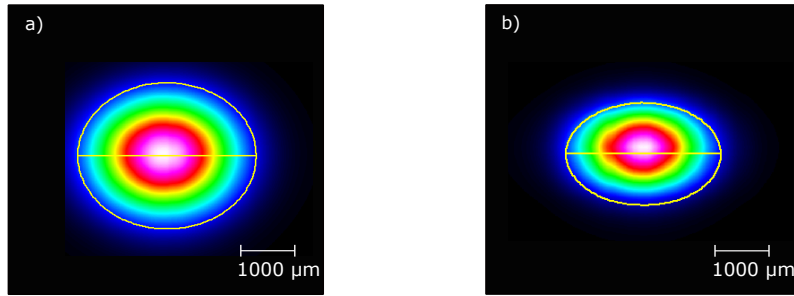

Figure 4.6: a) In-coupled beam profile measured after the mode-matching lenses. b) Out-coupled beam profile measured after the collimating lenses.

During high power operation, it was observed that MPC mirrors have beam-pointing instability. This instability limits the extended use of the MPC at high input laser powers as the spots are spaced closely and a minuscule shift in the beam pointing can result in clipping of the beam at the scraper positions. Snapshots of the spot pattern at increasing power values were compared to analyze a possible direction of misalignment. No particular direction was favored, alluding to the possibility of overheating mirrors. The spot pattern of the curved mirror at the low and high powers of the input laser is shown in Figure 4.9 a) and d). The second image is taken almost three hours after the first one, during a high-power run of the MPC.

For temporal post-compression, GTI mirrors, each with GDD of $-200 \, \text{fs}^2$, were set up, as shown in Figure 4.1. Measurements with 26, 34, 38, and 44 GTI mirror bounces were taken to find the ideal number of reflections required for maximum temporal compression as can be seen in Figure 4.8. A commercial autocorrelator (pulseCheck, APE GmbH) was employed for the intensity autocorrelation measurements. With 26 bounces, the pulse was compressed to $\sim 130 \, \text{fs}$. With 34 bounces, to $\sim 110 \, \text{fs}$. With 38 bounces, to $\sim 90 \, \text{fs}$ and with 44 bounces, the pulse was broader again to $\sim 110 \, \text{fs}$.
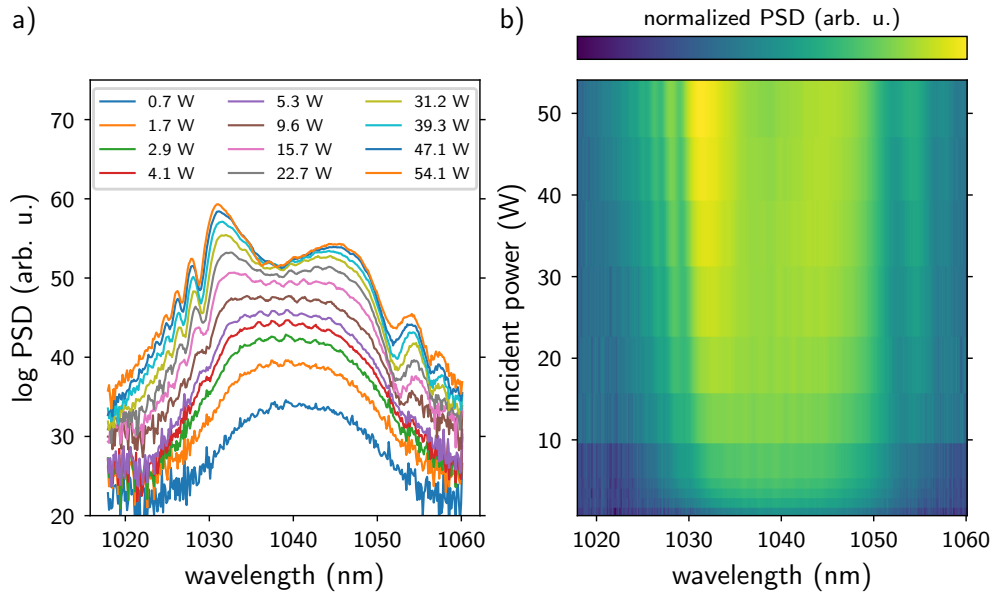
Figure 4.7: Spectral broadening with two plates of FS, each 6.35 mm thick, stacked in the MPC, as shown in Figure 4.4 a). a) Spectra of out-coupled light from the MPC plotted for increasing in-coupled powers in a logarithmic representation, with offsets for clarity. b) 2D plot of spectra using a linear colormap.
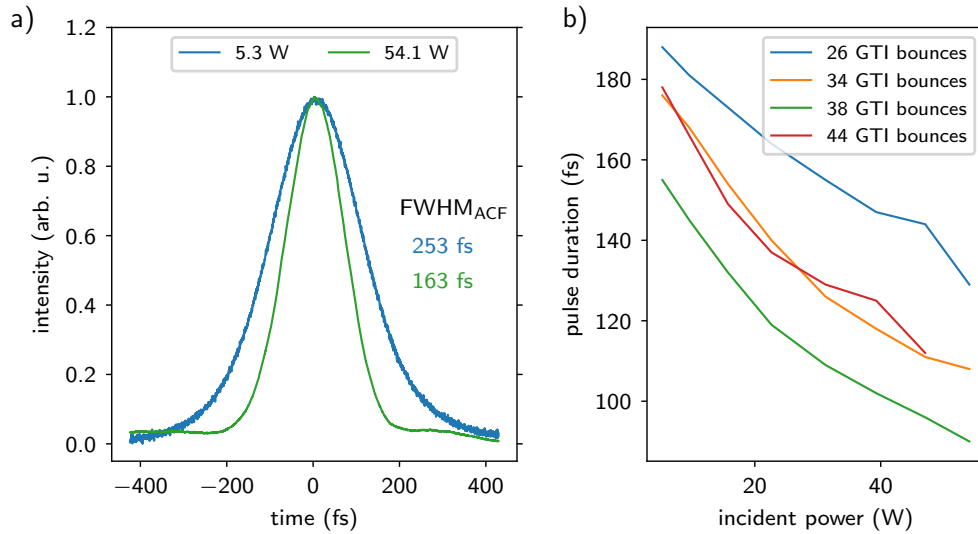
Figure 4.8: Temporal pulse compression in the FS multi-plate MPC with a subsequent chirped mirror pulse compressor. a) The autocorrelation function of the pulse after the MPC is shown for 38 bounces on three pairs of GTI mirrors for low and high input power. The stated values are the FWHM of the measured autocorrelation function. b) The pulse duration changes as a function of the input power for 26, 34, 38, and 44 GTI mirror bounces. It is stated as the FWHM of a fitted sech^2 temporal pulse shape. The shortest pulse duration $T_{\text{FWHM}} \approx 90\,\text{fs}$, which corresponds to a temporal pulse compression by a factor of two, is reached at maximum power with 38 GTI mirror bounces.
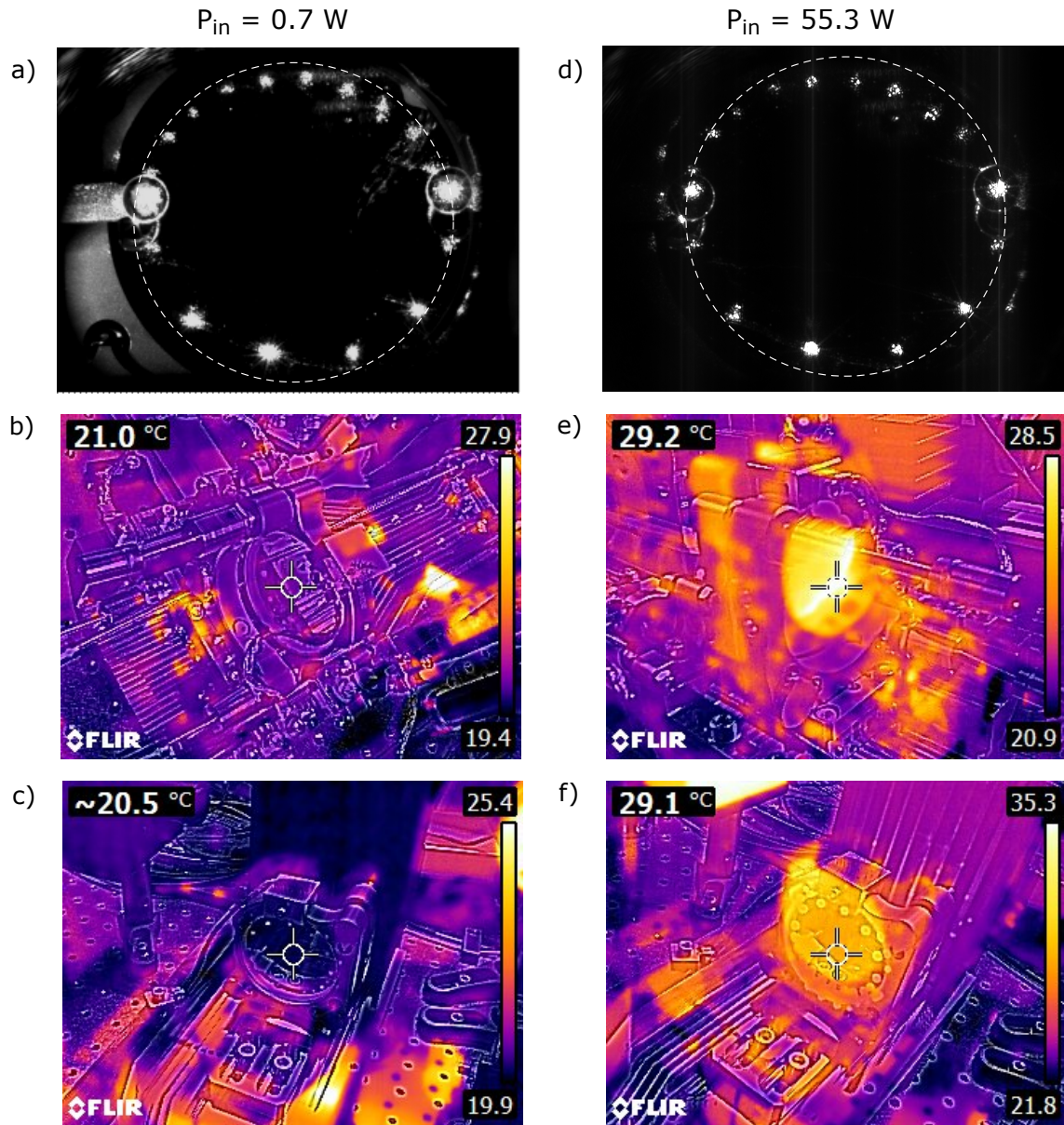
Figure 4.9: Input laser power $P_{in} = 0.7\,\text{W}$ for the left column and $P_{in} = 55.3\,\text{W}$ for the right column. a) and d) show the spot pattern on the left curved mirror. b) and e) show the thermal image of the back of the left curved mirror. c) and f) show the thermal image of the front of the right curved mirror.

Back-reflections from the FS plates that hit the mirror mounts, as shown in Figure 4.5, could be responsible for the excessive heating of the mounts. This in turn could be a reason for the poor beam-pointing of the mirrors. To prevent that, apertures could be installed in front of the mirrors in the future.
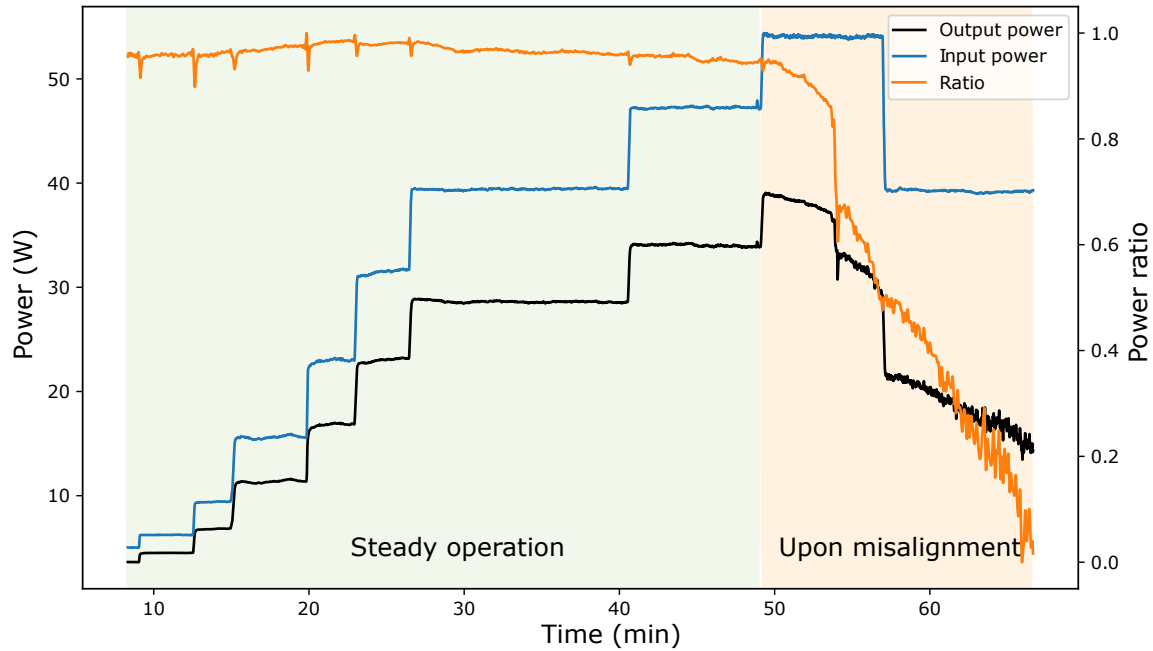
Figure 4.10: Monitored input (in blue) and output (in black) powers have been plotted along with their ratio (normalized value in orange). 34 passes through two FS plates are followed by 34 bounces on chirped mirrors. The MPC gives a steady response (shaded green) as the input power is increased. At $P_{\text{in}} \approx 54\,\text{W}$, the output power begins to drop due to misalignment in the cell. This is indicated by the falling black curve, at steady blue curve values, in the yellow-shaded region.

To measure the response of the cell at different input powers, the data from the two power meters illustrated in Figure 4.1 is plotted for 34 chirped bounces (Figure 4.10) and 44 chirped bounces (Figure 4.11). The input power is retrieved by multiplication of the value from the power meter at the input by the corresponding factor.

In Figure 4.10, at low input powers, the ratio of the two powers (orange line) is almost constant. This represents the steady response of the cell for the first fifty minutes. The small sharp peaks and dips in the orange line are due to the delay in MPC response. Unfortunately, at $P_{\text{in}} \approx 54\,\text{W}$, there is a sharp fall in the output power. This is due to misalignment in the cell. It is observed that at this power, the out-coupled spot from the second scraper mirror does not hit the out-coupling mirror in the center anymore. The mirror mount reaches a temperature of $\sim 100\,^{\circ}\text{C}$. The beam is clipped at the out-coupling window and hence the output power falls rapidly within a few minutes. This remains to be the case even after decreasing the input power to a lower value.

In Figure 4.11, again at low input powers, the ratio of the two powers is stable. The response begins to degrade slightly at input power range $30\,\text{W}$ to $50\,\text{W}$. At $P_{\text{in}} \approx 55\,\text{W}$, the cell begins to misalign again. It is hard to point at what position this happens, given the geometry of the cell.

For a consecutive measurement, the mirror mounts were connected to the base plate with copper braids for better heat dissipation, and the mirrors' temperatures were monitored with a thermal camera (E6xt, FLIR). The temperature changed from about $21\,^{\circ}\text{C}$ at $5\,\text{W}$ of input laser power (Figure 4.9 b) and c)) to about $29\,^{\circ}\text{C}$ at $55\,\text{W}$ (Figure 4.9 e)
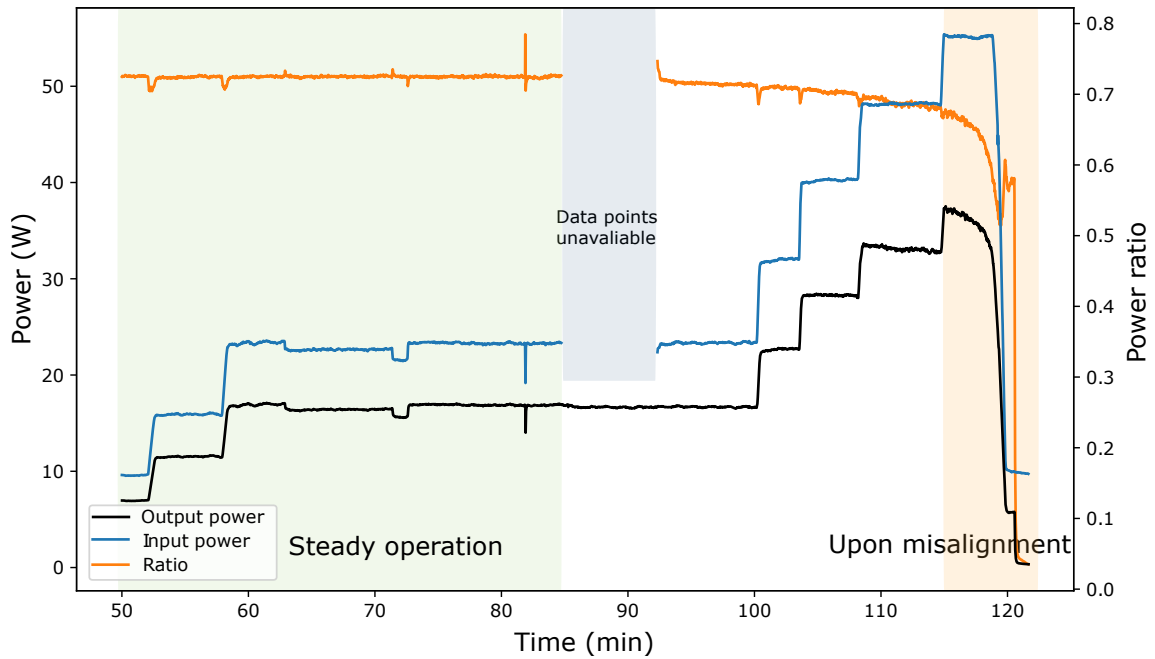
Figure 4.11: The power transmission for 34 passes through two FS plates followed by 44 bounces on chirped mirrors. MPC response is stable at low input powers (shaded green). The response at high powers can be seen in the unshaded region for a stepwise increase in the input power. At $P_{in} \approx 55\,\mathrm{W}$, the output power begins to drop due to misalignment in the cell.
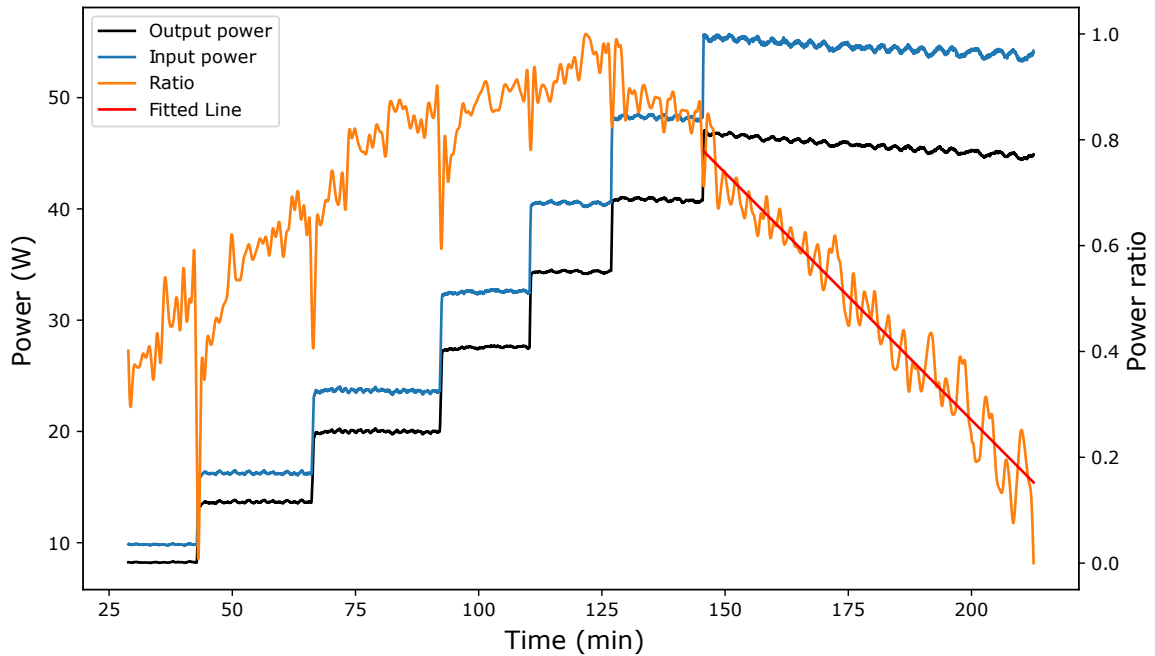
**Figure 4.12:** Transmission measurement carried out with cooling links attached to the mirror mounts for improved heat conductivity. The output power has been measured directly after the cell. The cell's response (in orange) improves with increasing power values before it begins to deteriorate at $P_{in} \approx 55\,\mathrm{W}$. The red fitted line represents the degradation of $\sim 0.9\,\%$ per minute.

and f)) within two hours. The measurement was carried out in ambient air, so heat is also dissipated by convective cooling. The transmission is plotted in Figure 4.12. It is evident that this is an improvement given that the cell does not misalign as in the two cases described before. However, a slow degradation of the cell's transmission is observed instead.

Three-plate assembly with FS

Finally, using the three-plate assembly, as shown in Figure 4.4 b), the MPC was aligned for 34 passes through the FS plates. In comparison to the two-plate assembly, the additional third plate was further away from the narrow focus of the MPC. Although an increase in broadening was expected with this addition, there was hardly any difference observed, as shown in Figure 4.13. This could have been due to the fact that there was not sufficient peak power at the position of the third plate to generate new frequencies by the nonlinear intensity-dependent process of SPM. The observed factors for this appear to be the rise in positive dispersion causing additional temporal broadening of the pulse and the substrate's transmission losses due to absorption and reflection.
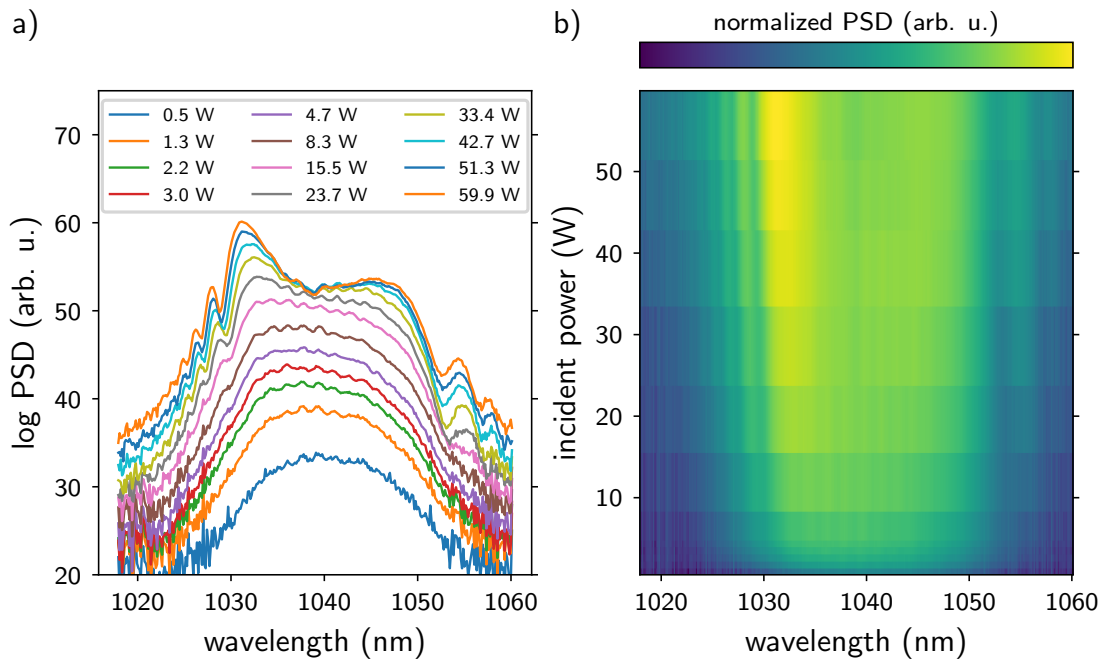
Figure 4.13: Spectral broadening measurement with three plates of 6.35 mm FS stacked in the MPC, as shown in Figure 4.4 b). a) Spectra of out-coupled light from the MPC plotted for increasing in-coupled powers in a logarithmic representation. b) The spectra are visualized in a 2D plot using a linear colormap.

4.3 Summary and outlook

Within the framework of this thesis, the nonlinear spectral broadening of sub-200 fs NIR ultrashort pulses was executed in a unique Herriott-type MPC geometry. This waveguide-like periodic multi-pass assembly consists of focusing elements (concave mirrors) and nonlinear media, providing an efficient measure for temporal compression in high average power systems at high repetition rates. Unlike the case of fiber-based spectral broadening typically performed in gas-filled capillaries, photonic bandgap, or Kagome-type hollow-core photonic-crystal fibers, the multi-pass geometry offers spectral broadening in a highly robust and simple manner.

A dispersion tunable MPC was assembled and the first measurements of spectral broadening and post-compression were carried out. The flexible optomechanical design of the cell provides access to a wide working range of multiple important cell parameters. Nevertheless, the laser alignment in the cell requires meticulous effort to make sure that the back-and-forth propagation gives a circularly geometric spot pattern. High-power ultrashort laser pulses with an average power of over 75 W are provided from a Yb:fiber-based amplifier system. A periscope is designed to adjust for the beam height required for in-coupling in the MPC. To ensure mode-matching of the in-coupled beam, a system of lenses focuses the beam to a waist of $\sim 95\,\mu$m at the center of the cell. The out-coupled beam is collimated by another set of lenses. The lenses are mounted on rails, to allow for fine adjustments, which are further mounted on a sturdy elevated breadboard assembly to allow for in-coupling to the MPC. The 2-inch mirrors placed at a distance of $\sim 495\,$mm allow for 1.5 half circles which correspond to 34 passes through the nonlinear medium.

FS was employed in a multi-plate configuration to avoid disruptive self-focusing effects common at high peak intensities. Two-and three-plate assemblies were tested experimentally. The emergence of spectral wings at high power represented spectral broadening due to SPM. In comparison to the two-plate assembly, the three-plate assembly did not result in a significantly enhanced spectral broadening. This might be attributed to the plate positions being distant from the focus, which limits the peak intensities achieved. Furthermore, subsequent accumulation of temporal broadening due to dispersion effects prevented high spectral broadening ratios in both cases.

Temporal post-compression was performed by placing multiple pairs of chirped mirrors outside the MPC to achieve sub-100 fs pulses. Intensity autocorrelation of the pulses was performed for four sets of configurations differing in the number of bounces off the chirped mirrors with GDD of $-200\,$fs^2 each. For 38 reflections, the shortest duration of $\sim 90\,$fs, corresponding to a temporal compression of the input pulses almost by a factor of two is achieved. A new FROG setup is currently being built to characterize the spectral phase of the out-coupled pulses [63] since the existing setup operates at a slow pace.

The initial high power measurements were faced with poor beam pointing. This could have been due to improper alignment. Improving on that, measurements of the long-term average power stability were carried out for over one hour yielding better results. The MPC mirrors were monitored continuously by a camera to inspect the spot pattern for pointing drifts as the input power was scaled.

Until now, MPCs have primarily functioned under conditions of zero or normal dispersion. Nonetheless, the appeal of utilizing MPCs to broaden the spectrum gains more intrigue when dealing with strong peak power levels, particularly when paired with operation within the

anomalous dispersion range. This is the zone where effects such as self-compression, Raman soliton self-frequency shifting, supercontinuum generation, and other intricate nonlinear behaviors are projected to become active [64]. This can be incorporated in multiple ways. The broadening substrate, and the mirror coatings [65] can provide dispersion compensation.

We utilized the anomalous dispersion of KDP crystals at 1030 nm and simulated temporal compression by a factor of ~ 5 in a single broadening stage without necessitating subsequent dispersive optics. This corresponds to an increase in peak power by a factor of two. Experiments of spectral broadening and self-compression using KDP crystals of 3 mm and 4 mm were inconclusive given the damage of the crystals already at very low input power well below the critical power for self-focusing. Inspection of the cracks under a microscope signified no signs of mechanical stress due to mounting and thus the most probable cause was sought to be a manufacturing defect.

Another way of implementing self-compression in the cell is to utilize a GTI mirror which compensates for the normal dispersion of the broadening media. This has already been implemented using chirped curved mirrors with a GDD of $-100\,\text{fs}^2$ and temporal compression measurements will soon be carried out. This would benefit significantly since high peak powers could be maintained throughout the back-and-forth propagation of the beam and fewer passes would be required to achieve the desired compression ratios.

To complement the self-compression regime of an anomalous dispersive crystal or a mirror coating, the cell is designed to operate under vacuum and at high pressures of inert gases. This enables the precise adjustment of dispersion by varying the gas pressure, thereby adapting to the desired spectral broadening ratios.

Bulk MPCs are typically operated in the critical self-focusing regime where the effect of Kerr-lensing is very strong. This can result in a weak guiding effect within a single pass [66]. Furthermore, refraction in gases which causes oscillations of the beam size over the roundtrips upon nonlinear propagation is also ignored [67]. While mode-matching can be adjusted during experiments, beginning with the linear stationary beam, a deeper comprehension of the influence of nonlinearity on the caustic would be beneficial in refining this delicate procedure. This understanding would aid in achieving better homogeneity of the beam sizes at the mirrors. Hence improved input beam coupling could be implemented as a prospective upgrade.

MPCs exhibit better power efficiency than other methods of pulse compression [46]. Their robustness makes them insensitive to beam pointing and even small mode mismatches without transmission losses [68]. The transmission then majorly depends on the optics used in the cell. Without any nonlinear medium, at 34 passes, our cell has a throughput of $\sim 85\%$. With 34 passes through the AR-coated FS plates, our cell has a throughput of $\sim 81\%$ with two and $\sim 74\%$ with three plates. This is hoped to be improved by better AR-coated mirrors.

The distinct configuration of the cell enables operation using both gas-filled and bulk plate approaches. Moreover, when in closed-cell operation, precision alignment of optics within the cell is facilitated by custom-built rotary feedthroughs. Since the desired broadening in our experiment is currently limited to a bandwidth of $\sim 90\,\text{nm}$ due to the dispersion effects in the cavity, the targeted pulse duration is $\sim 30\,\text{fs}$. Anticipating the forthcoming upgrades to the MPC, we hold optimistic prospects of achieving this goal in the near future.

The utilization of shorter pulses holds multifaceted benefits across various applications in our lab. First, in a novel polarization-insensitive fsEC that allows photoelectron tomography at 100 MHz repetition rate using VMI, shorter pulses would provide better electron yield in the process of MPI. Second, in an intra-cavity HHG based XUV frequency comb laser, higher peak intensities from shorter pulses would enable more efficient nonlinear HHG. With an increased cut-off energy, even higher-order harmonics could be produced. The accompanying broader spectra would be transferred to the XUV regime and allow access to more HCI transitions. In consequence, nonlinear pulse compression by the MPC would stand to be a significant advancement facilitating precision spectroscopy of HCIs and the measurement of potential variations in the fine-structure constant.

Bibliography

[1]   K. Beloy et al. "Frequency ratio measurements at 18-digit accuracy using an optical clock network". In: *Nature* 591.7851 (2021), pp. 564–569.

[2]   H. Bekker et al. "Detection of the 5p-4f orbital crossing and its optical clock transition in Pr^{9+}". In: *Nature Communications* 10.1 (2019).

[3]   T. R. Kallman and P. Palmeri. "Atomic data for x-ray astrophysics". In: *Reviews of Modern Physics* 79.1 (2007), pp. 79–133.

[4]   H. Chen et al. "Soft-x-ray spectra of highly charged Kr ions in an electron beam ion trap". In: *Physical Review E* 65.5 (2002).

[5]   J. R. Crespo López-Urrutia and Z. Harman. "Emission and Laser Spectroscopy of Trapped Highly Charged Ions in Electron Beam Ion Traps". In: *Springer Tracts in Modern Physics*. Springer Berlin Heidelberg, 2014, pp. 315–373.

[6]   L. Schmöger et al. "Deceleration, precooling, and multi-pass stopping of highly charged ions in Be^+ Coulomb crystals". In: *Review of Scientific Instruments* 86.10 (2015), p. 103111.

[7]   J. Nauta. "An extreme-ultraviolet frequency comb enabling frequency metrology with highly charged ions". Ruprecht-Karls-Universität, Heidelberg, 2020. PhD thesis.

[8]   S. B. Utter et al. "Position and size of the electron beam in the high-energy electron beam ion trap". In: *Nuclear Instruments and Methods in Physics Research Section A: Accelerators, Spectrometers, Detectors and Associated Equipment* 428.2-3 (1999), pp. 276–283.

[9]   P. O. Schmidt et al. "Spectroscopy using quantum logic". In: *Science* 309.5735 (2005), pp. 749–752.

[10] J. Stark et al. "An ultralow-noise superconducting radio-frequency ion trap for frequency metrology with highly charged ions". In: *Review of Scientific Instruments* 92.8 (2021), p. 083203.

[11] A. Cingöz et al. "Direct frequency comb spectroscopy in the extreme ultraviolet". In: *Nature* 482.7383 (2012), pp. 68–71.

[12] D. C. Yost et al. "Power optimization of XUV frequency combs for spectroscopy applications [Invited]". In: *Optics Express* 19.23 (2011), p. 23483.

[13] R. J. Jones et al. "Phase-Coherent Frequency Combs in the Vacuum Ultraviolet via High-Harmonic Generation inside a Femtosecond Enhancement Cavity". In: *Physical Review Letters* 94.19 (2005).

[14] D. Z. Kandula et al. "Extreme Ultraviolet Frequency Comb Metrology". In: *Physical Review Letters* 105.6 (2010).

[15] T. Fortier and E. Baumann. "20 years of developments in optical frequency comb technology and applications". In: *Communications Physics* 2.1 (2019).

[16] J.-H. Oelmann. "Highly nonlinear light-matter interaction using cavity-enhanced frequency combs". Ruprecht-Karls-Universität, Heidelberg, 2023. PhD thesis.

[17] D. J. Jones et al. "Carrier-Envelope Phase Control of Femtosecond Mode-Locked Lasers and Direct Optical Frequency Synthesis". In: *Science* 288.5466 (2000), pp. 635–639.

[18] S. A. Diddams et al. "An Optical Clock Based on a Single Trapped Hg Ion". In: *Science* 293.5531 (2001), pp. 825–828.

[19] T. Udem et al. "Optical frequency metrology". In: *Nature* 416.6877 (2002), pp. 233–237.

[20] T. Brabec and F. Krausz. "Intense few-cycle laser fields: Frontiers of nonlinear optics". In: *Reviews of Modern Physics* 72.2 (2000), pp. 545–591.

[21] J. J. Macklin et al. "High-order harmonic generation using intense femtosecond pulses". In: *Physical Review Letters* 70.6 (1993), pp. 766–769.

[22] A. L'Huillier et al. "Higher-order harmonic generation in xenon at 1064 nm: The role of phase matching". In: *Physical Review Letters* 66.17 (1991), pp. 2200–2203.

[23] C. Gohle et al. "A frequency comb in the extreme ultraviolet". In: *Nature* 436.7048 (2005), pp. 234–237.

[24] K. J. Schafer et al. "Above threshold ionization beyond the high harmonic cutoff". In: *Physical Review Letters* 70.11 (1993), pp. 1599–1602.

[25] P. B. Corkum. "Plasma perspective on strong field multiphoton ionization". In: *Physical Review Letters* 71.13 (1993), pp. 1994–1997.

[26] J. Nauta et al. "100 MHz frequency comb for low-intensity multi-photon studies: intra-cavity velocity-map imaging of xenon". In: *Optics Letters* 45.8 (2020), p. 2156.

[27] F. Lindner et al. "High-order harmonic generation at a repetition rate of 100 kHz". In: *Physical Review A* 68.1 (2003).

[28] A. Harth et al. "Compact 200 kHz HHG source driven by a few-cycle OPCPA". In: *Journal of Optics* 20.1 (2017), p. 014007.

[29] A. Rundquist et al. "Phase-Matched Generation of Coherent Soft X-rays". In: *Science* 280.5368 (1998), pp. 1412–1415.

[30] S. Angstenberger. "Design of a setup for flexible, dispersion-compensated nonlinear femtosecond laser pulse compression adapted to an extreme ultraviolet frequency comb". Ruprecht-Karls-Universität, Heidelberg. MA thesis. 2021.

[31] P. A. Franken et al. "Generation of Optical Harmonics". In: *Physical Review Letters* 7.4 (1961), pp. 118–119.

[32] T. Schneider. *Nonlinear Optics in Telecommunications.* Springer Berlin Heidelberg, 2004.

[33] V. Parodi et al. "Nonlinear Optical Microscopy: From Fundamentals to Applications in Live Bioimaging". In: *Frontiers in Bioengineering and Biotechnology* 8 (2020).

[34] N. Akhmediev et al. "Recent progress in investigating optical rogue waves". In: *Journal of Optics* 15.6 (2013), p. 060201.

[35] P. L. Kelley. "Self-Focusing of Optical Beams". In: *Physical Review Letters* 15.26 (1965), pp. 1005–1008.

[36] M. Sheik-Bahae et al. "Sensitive measurement of optical nonlinearities using a single beam". In: *IEEE Journal of Quantum Electronics* 26.4 (1990), pp. 760–769.

[37] R. W. Boyd. *Nonlinear Optics.* Academic Press, 2008.

[38] P. Kabaciński et al. "Nonlinear refractive index measurement by SPM-induced phase regression". In: *Optics Express* 27.8 (2019), p. 11018.

[39] G. Genty et al. "Nonlinear envelope equation modeling of sub-cycle dynamics and harmonic generation in nonlinear waveguides". In: *Optics Express* 15.9 (2007), p. 5382.

[40] J. K. Ranka et al. "Visible continuum generation in air–silica microstructure optical fibers with anomalous dispersion at 800 nm". In: *Optics Letters* 25.1 (2000), p. 25.

[41] G. P. Agrawal. *Nonlinear Fiber Optics*. Electronics & Electrical. Elsevier Science, 2007.

[42] S. Hädrich et al. "Energetic sub-2-cycle laser with 216 W average power". In: *Optics Letters* 41.18 (2016), p. 4332.

[43] J. C. Travers et al. "Ultrafast nonlinear optics in gas-filled hollow-core photonic crystal fibers [Invited]". In: *Journal of the Optical Society of America B* 28.12 (2011), A11.

[44] J. Schulte et al. "Nonlinear pulse compression in a multi-pass cell". In: *Optics Letters* 41.19 (2016), p. 4511.

[45] D. Herriott et al. "Off-Axis Paths in Spherical Mirror Interferometers". In: *Applied Optics* 3.4 (1964), p. 523.

[46] A.-L. Viotti et al. "Multi-pass cells for post-compression of ultrashort laser pulses". In: *Optica* 9.2 (2022), p. 197.

[47] N. Milosevic et al. "Optical pulse compression: bulk media versus hollow waveguides". In: *Optics Letters* 25.9 (2000), p. 672.

[48] A. Sennaroglu and J. Fujimoto. "Design criteria for Herriott-type multi-pass cavities for ultrashort pulse lasers". In: *Optics Express* 11.9 (2003), p. 1106.

[49] P. Russbueldt et al. "Compact diode-pumped 11 kW Yb:YAG Innoslab femtosecond amplifier". In: *Optics Letters* 35.24 (2010), p. 4169.

[50] M. Kaumanns et al. "Multipass spectral broadening of 18 mJ pulses compressible from 13 ps to 41 fs". In: *Optics Letters* 43.23 (2018), p. 5877.

[51] G. Jargot et al. "Self-compression in a multipass cell". In: *Optics Letters* 43.22 (2018), p. 5643.

[52] P. Redman et al. *gnlse-python: Open Source Software to Simulate Nonlinear Light Propagation In Optical Fibers*. 2021.

[53] J. M. Dudley and J. R. Taylor, eds. *Supercontinuum Generation in Optical Fibers*. Cambridge University Press, 2010.

[54] T. Harimoto and K. Yamakawa. "Self compression of Yb-doped solid-state lasers by combination of self-phase modulation and group-velocity dispersion in KDP crystal". In: *Optics Express* 15.23 (2007), p. 15438.

[55] D. Strickland and G. Mourou. "Compression of amplified chirped optical pulses". In: *Optics Communications* 56.3 (1985), pp. 219–221.

[56] K. Fritsch et al. *Spectral broadening in convex-concave multipass cells*. 2022.

[57] A. M. Kowalevicz et al. "Design principles of q-preserving multipass-cavity femtosecond lasers". In: *Journal of the Optical Society of America B* 23.4 (2006), p. 760.

[58] Y.-C. Cheng et al. "Supercontinuum generation in a multi-plate medium". In: *Optics Express* 24.7 (2016), p. 7224.

[59] M. Müller et al. "Multipass cell for high-power few-cycle compression". In: *Optics Letters* 46.11 (2021), p. 2678.

[60]   H. Unold. "Modenanpassung für eine Multipasszelle zur spektralen Verbreiterung ultrakurzer Laserpulse". Bachelor thesis. Ruprecht-Karls-Universität, Heidelberg, 2023.

[61]   M. Hanna et al. "Nonlinear beam matching to gas-filled multipass cells". In: *OSA Continuum* 4.2 (2021), p. 732.

[62]   N. Daher et al. "Spectral compression in a multipass cell". In: *Optics Express* 28.15 (2020), p. 21571.

[63]   F. Sieber. In preparation: Master's thesis. Ruprecht-Karls-Universität, Heidelberg.

[64]   J. M. Dudley et al. "Supercontinuum generation in photonic crystal fiber". In: *Reviews of Modern Physics* 78.4 (2006), pp. 1135–1184.

[65]   S. Gröbmeyer et al. "Self-compression at 1 μm wavelength in all-bulk multi-pass geometry". In: *Applied Physics B* 126.10 (2020).

[66]   M. Seidel et al. "Factor 30 Pulse Compression by Hybrid Multipass Multiplate Spectral Broadening". In: *Ultrafast Science* 2022 (2022).

[67]   M. Hanna et al. "Hybrid pulse propagation model and quasi-phase-matched four-wave mixing in multipass cells". In: *Journal of the Optical Society of America B* 37.10 (2020), p. 2982.

[68]   A. Vernaleken et al. "Method and arrangement for spectral broadening of laser pulses for non-linear pulse compression". In: EP3143669A1 (2017). US Patent [9,847,615].

Acronyms

MPC   multi-pass cell
XUV   extreme ultraviolet
HCI   highly charged ion
EBIT   electron beam ion trap
OFC   optical frequency comb
NIR   near-infrared
YAG   yttrium aluminium garnet
HHG   high-harmonic generation
fsEC   femtosecond enhancement cavity
MPI   multi-photon ionization
VMI   velocity-map imaging
SPM   self-phase modulation
GVD   group velocity dispersion
TOD   third-order dispersion
GNLSE   generalized nonlinear Schrödinger equation
NLSE   nonlinear Schrödinger equation
PDE   partial differential equation
KDP   potassium dihydrogen phosphate
GDD   group delay dispersion
FROG   frequency-resolved optical gating
FS   fused silica
HR   high reflection
AR   anti-reflection
GTI   Gires-Tournois-Interferometer
SHG   second-harmonic generation
FWHM   full width half maxima

Acknowledgements

Declaration

Ich versichere, dass ich diese Arbeit selbstständig verfasst habe und keine anderen als die angegebenen Quellen und Hilfsmittel benutzt habe.

Heidelberg, den   29.08.23 ....